The Astrophysical Journal, 913:124 (23pp), 2021 June 1 https://doi.org/10.3847/1538-4357/abf3c1
© 2021. The American Astronomical Society. All rights reserved.

Eruptivity in Solar Flares: The Challenges of Magnetic Flux Ropes

Pei Hsuan Lin[1], Kanya Kusano[1], and K. D. Leka[1,2]
[1] Nagoya University, Furo-cho, Chikusa-ku, Nagoya, Aichi, 464-8601, Japan; jnes40722@isee.nagoya-u.ac.jp
[2] NorthWest Research Associates, Inc., Boulder, CO, USA
Received 2020 December 25; revised 2021 March 29; accepted 2021 March 29; published 2021 June 2

Abstract

Two new schemes for identifying field lines involved in eruptions, the *r*-scheme and *q*-scheme, are proposed to analyze the eruptive and confined nature of solar flares, as extensions to the original r_m scheme proposed in Lin et al. Motivated by three solar flares originating from NOAA Active Region 12192 that are misclassified by r_m, we introduce refinements to the *r*-scheme employing the "magnetic twist flux" to approximate the force balance acting on a magnetic flux rope (MFR); in the *q*-scheme, the reconnected field is represented by those field lines that anchor in the flare ribbons. Based on data obtained by the Solar Dynamics Observatory/Helioseismic and Magnetic Imager, the coronal magnetic field for 51 flares larger than M5.0 class, from 29 distinct active regions, is constructed using a nonlinear force-free field extrapolation model. Statistical analysis based on linear discriminant function analysis is then performed, revealing that despite both schemes providing moderately successful classifications for the 51 flares, the coronal mass ejection-eruptivity classification for the three target events can only be improved with the *q*-scheme. We find that the highly twisted field lines and the flare-ribbon field lines have equal average force-free constant α, but all of the flare-ribbon-related field lines are shorter than 150 Mm in length. The findings lead us to conclude that it is challenging to distinguish the MFR from the ambient magnetic field using any quantity based on common magnetic nonpotentiality measures.

Unified Astronomy Thesaurus concepts: Solar magnetic fields (1503); Solar physics (1476); Solar active regions (1974); Solar coronal mass ejections (310)

1. Introduction

Solar eruptions are phenomena wherein free magnetic energy stored in the solar corona is released through magnetic reconnection (Priest & Démoulin 1995) and magnetohydrodynamic (MHD) instabilities. Solar eruptions usually originate from those magnetic fields with high nonpotentiality. In particular, coronal mass ejections (CMEs) and solar flares are critical topics in solar physics because they are the main driver of space weather. CMEs often follow flares (Munro et al. 1979; Webb & Hundhausen 1987; Sheeley et al. 1983), and it is commonly believed that CMEs and flares are different manifestations of the same magnetic energy release process in the corona (e.g., Harrison 1995, 2003; Lin & Forbes 2000; Zhang et al. 2001; Priest & Forbes 2002; Zhang & Dere 2006; Maričić et al. 2007; Temmer et al. 2008; Cheng et al. 2010), yet observations have shown that there is in fact no one-to-one relationship between these phenomena. For instance, the solar active region (AR) 12192, while an extremely large AR, generated a succession of CME-less flares (Chen et al. 2015; Sun et al. 2015; Thalmann et al. 2015). Some studies refer to solar energetic events for which only flares are detected as "failed events" or "confined events" as we use in this study (Moore et al. 2001), implying that coronal material failed to escape from the solar surface (e.g., Ji et al. 2003; Alexander et al. 2006; Török & Kliem 2005; Liu et al. 2009; Kuridze et al. 2013; Filippov 2020; Kushwaha et al. 2015). Conversely, we refer to flares with CMEs as "eruptive flares."

Magnetic flux ropes (MFRs) are believed to comprise the cores of CMEs, although to date there is no standard definition of an MFR. The existence of MFRs inside CMEs is implied by structures visible in coronagraph observations near the Sun (Chen et al. 1997; Dere et al. 1999; Vourlidas et al. 2013) and by in situ observations of a CME counterpart in interplanetary space, helical "magnetic clouds" (Burlaga 1991). A general definition of an MFR describes a core structure participating in the magnetic reconnection associated with the eruption, usually appearing as twisted field lines and anchored across strong polarity inversion lines (PILs) as seen in maps of the photospheric radial magnetic field. A "well-formed MFR" may include the requirement of high twist; for example, Duan et al. (2019) and Liu et al. (2016) used $|T_w| \geqslant 1$. However, in this study, we relax the requirement on twist and do not strictly require a well-defined axis and consider an MFR as simply twisted field lines, even if weakly twisted, that display a coherent structure.

An MFR in an AR is regarded to play an important role in the eruption process. For instance, MFR is an important element of the generally accepted CSHKP model (Carmichael 1964; Sturrock 1966; Hirayama 1974; Kopp & Pneuman 1976); in the tether-cutting model (Moore et al. 2001) and the breakout model (Antiochos et al. 1999), the MFR is described by the sheared arcades. An MHD instability is considered one possible eruption mechanism. The torus instability (TI; Kliem & Török 2006; Démoulin & Aulanier 2010) is widely accepted as a possible CME initiation mechanism. TI suggests that if an MFR is located within a magnetic field that decays (with height) more quickly than a certain criterion, then it is possible to erupt and generate the CME (e.g., Fan & Gibson 2007; Liu 2008; Guo et al. 2010; Nindos et al. 2012; Jing et al. 2015; Wang et al. 2017; Baumgartner et al. 2018; Duan et al. 2019). In a similar approach to that used for TI-focused analysis, one can generalize to the "relative nonpotentiality" of an MFR as the ratio of magnetic flux (or other physical quantities) in a preexisting MFR to that in the surrounding magnetic structures. A larger relative nonpotentiality indicates a higher probability for an MFR to erupt. A variety of schemes have been introduced to quantitatively evaluate the relative

nonpotentiality: the ratio of the magnetic field strength between the MFR and its background (Wang & Zhang 2007; Liu 2008; Cheng et al. 2011; Sun et al. 2015; Thalmann et al. 2015); the percentage of reconnected flux inferred from associated flare ribbons (Toriumi et al. 2017); the magnetic flux in the highly twisted region relative to its immediate ambient field (Lin et al. 2020); the magnetic energy and currents stored in the core region compared to the whole AR (Sun et al. 2015); and the ratio of current-carrying to total helicity (Thalmann et al. 2019). All results show a tendency for the strength of the flux rope relative to the surrounding field to be crucial for deciding the eruptive nature (or not) of the associated MFR. Moreover, the topology of the magnetic field may be important regarding an event's eruptivity: some studies suggest that an open-field structure can facilitate the formation of CMEs, as opposed to a closed configuration that will instead "strap down" a rising MFR (e.g., Antiochos et al. 1999; Ji et al. 2003; Chintzoglou et al. 2017; DeRosa & Barnes 2018).

Combining the concepts of relative nonpotentiality and the geometry of the coronal magnetic field, Lin et al. (2020, hereafter Paper I) examined 51 flare events with a newly proposed algorithm to identify magnetic flux systems that either comprise or will form an MFR and its relation to its surroundings. This r_m scheme demonstrated a moderate ability to correctly assign the eruptive (or confined) nature to these events. The results from all of these studies imply that it is required to consider both the nonpotential and background components of the magnetic field when attempting to determining the eruptive capability of an AR.

Obviously, evaluating the "relative nonpotentiality" of an MFR requires correctly identifying the location and the volume of the MFR. However, because there is still no general definition of an MFR, it is nontrivial to accurately identify one from a magnetic field construction, as well as subsequently quantifying the reconnected flux related to it. Present approaches used to infer the presence of an MFR and estimate the amount of event-related magnetic reconnection are based primarily on the magnetic twist number. For instance, Muhamad et al. (2018) and Paper I used the magnetic flux associated with field lines displaying twist over a certain threshold as the approximation of the reconnected flux contributed by an MFR. Duan et al. (2019) and Liu et al. (2016) rendered a channel with the twist number over a certain threshold as the representation of MFRs. Signatures of MFRs in magnetic field structures can be based on a topological definition, such as requiring a bald patch separatrix surface (Gibson & Fan 2006); this definition was applied by Green & Kliem (2009) to interpret the soft X-ray sigmoid observation. Additionally, Pagano et al. (2019) proposed the "flux rope ejection metric," which includes an estimate of both magnetic field twist and Lorentz force, to evaluate the possibility of an MFR's existence and its likelihood of erupting. In short, identifying the signatures of MFRs before solar eruptions is still under debate, with numerous methodologies under investigation, especially for the question of identifying the frontier that separates an MFR itself from its immediate environs and their respective contribution to whether a flare will be accompanied by a CME.

The parameter r_m proposed in Paper I is the ratio of magnetic flux in distinct areas, defined so as to approximate the force balance of an eruption-imminent MFR. We showed that r_m was able to independently determine the association of a flare with an accompanying CME, but only at a moderate level. In this context, three events originating from NOAA AR 12192 failed to be correctly assigned. With this motivation, we further investigate these events here and reexamine the r_m scheme proposed by Paper I to investigate further the mechanism of CME initialization in the context of solar flares.

This paper is organized as follows: in Section 2, we review r_m and describe its failure to classify three confined events from NOAA AR 12192. In Section 3, we analyze what factor(s) cause these three misclassifications, propose and apply different approaches that each deploy different descriptions of the relevant flux systems, and evaluate their classification results. Next, the results are discussed in Section 4 in the context of MHD instabilities and the flares' behaviors. Finally, Section 5 summarizes and concludes this research. Of note, we include additional details on the analysis and uncertainties in the Appendices.

2. Data, Review of Analysis Methods, and Target Events

We aim to investigate further the mechanism of CME initialization through these three incorrectly classified events as they appear in the r_m scheme. We apply an identical methodology used in Paper I such that we can make a meaningful comparison with the conclusions from the previous paper. In this section, we review the r_m parameter proposed by Paper I and introduce the data and methods used in that study. An overview of the three target events, originating from NOAA active region 12192, is presented in this section.

2.1. Event List, Data, and Method

Here as in Paper I, we use an event list initiated by Toriumi et al. (2017) of 51 flare events from 29 active regions (see Appendix A). These flares all have Geostationary Operational Environmental Satellite (GOES) SXR peak magnitudes in 1–8 Å bandpass $\geqslant 5 \times 10^{-5}\,\mathrm{W\,m^{-2}}$ (M5.0) and were located within 45° of disk center. Among these 51 flare events, 33 flares are classified as eruptive and 18 events are classified as confined. The Solar Dynamics Observatory (SDO)/Helioseismic and Magnetic Imager (HMI) provides maps of the vector magnetic field from the Spaceweather HMI Active Region Patches (SHARPs `hmi.sharp_cea_720s`; Bobra & Ilonidis 2016)[3] that are employed as boundary conditions to derive the three-dimensional coronal magnetic field. We use the `hmi.sharp_cea_720s` data series, in which the vector magnetic field data has been remapped to a Lambert Cylindrical Equal-Area (CEA) projection and decomposed into B_r, B_θ, and B_ϕ components. Additionally, data from SDO/Atmospheric Imaging Assembly (AIA; Lemen et al. 2011) are used to confirm coronal loops, and the 1600 passband observations are used to identify the flare ribbons. Because the computation of r_m requires the geometrical information of the coronal magnetic field, in this study, we perform the identical nonlinear force-free field (NLFFF) extrapolation method as used by Paper I; readers are referred to Appendix B for more details.

2.2. Magnetic Twist (T_w)

After obtaining the 3D magnetic field construct from the NLFFF extrapolation, we calculate the twist number T_w in the derived data cube. T_w can measure how many turns of two

[3] http://jsoc.stanford.edu

close field lines wind about each other (Berger & Prior 2006), which is computed as

$$T_w = \frac{1}{4\pi}\int \alpha dl. \quad (1)$$

Here, dl is a line element along a field line and α is the associated force-free parameter:

$$\alpha = \frac{\nabla \times \boldsymbol{B}\cdot\boldsymbol{B}}{|\boldsymbol{B}|^2}. \quad (2)$$

T_w is derived by integrating α over all of the voxels along each field line from one photospheric footpoint to the other. Here we apply the α values derived from the NLFFF boundary. In a force-free construct, the α parameter is constant along each field line; in practice, we linearly integrate the α along the field lines and divide by the field line length, making the α at the conjugate footpoints agree with the NLFFF assumptions. Each footpoint then has a unique T_w assigned.

T_w can be an approximation of the winding of field lines about an axis field line without resorting to the MFR's axis, but only under certain conditions. Liu et al. (2016) have proved that Equation (1) can be a reliable approximation of the classical definition (Equation (12) in Berger & Prior 2006) when T_w is located near the axis of a nearly cylindrically symmetrical MFR (i.e., where T_w is concentrating). Leka et al. (2005) used a "blind test" to demonstrate that directly deriving T_w from a photospheric magnetogram was only valid in the vicinity near the MFR's axis, likely the location of the local maximum $|T_w|$. Because we are calculating T_w from the NLFFF coronal model and not directly from the boundary photospheric magnetogram, the proximity (or not) to the MFR axis is not a constraint for our study. For each NLFFF construction, we trace the field lines from multiple locations within each pixel on the lower boundary and compute the corresponding T_w at each derived field line. Thus, we produce a map of T_w (which is dubbed "twist map") for each field line and its photospheric footpoints. With this twist map and NLFFF data cube, we calculate the quantities necessary for the subsequent analysis.

2.3. Concept and Estimation of r_m

The r_m parameter presented in Paper I was designed to estimate the likelihood that a flare would be eruptive. r_m arises from the concept that a CME will erupt if the force that drives the eruption of the MFR overtakes the magnetic confinement from its surroundings. Paper I approximates the force balance by the ratio of magnetic flux, invoking the assumption that the low corona generally has $\beta < 1$, or magnetically dominated plasma (Gary 2001). Li et al. (2020) analyzed 322 large flares and found that eruptive events occur less frequently from ARs with a total unsigned magnetic flux larger than 1.0×10^{23} Mx, implying that strong fields (i.e., large magnetic flux) generally tend to confine eruptions. In a system composed of an MFR and the magnetic field in its immediate neighborhood, the associated r_m in this system is defined by

$$r_m = \frac{\Phi_{T_w \geqslant T_c}}{\Phi_{T_w \geqslant T_c} + \Phi_{\rm surrounding}}, \quad (3)$$

where T_c is an imposed threshold of the twist number. $\Phi_{T_w \geqslant T_c}$ is used because field lines with a higher twist are more likely to cause internal magnetic reconnection and trigger an eruption than less-twisted magnetic flux (Démoulin & Aulanier 2010). In other words, the magnetic flux in the area with T_w higher than the T_c threshold is regarded as representing the total reconnected flux relevant for an eruption. The chosen value of T_c depends on the purpose of the study. For instance, Muhamad et al. (2018) used $T_c = 0.5$ to study the onset condition for solar flares. To analyze the CME generation, Paper I focused on the total reconnected flux contributed by an MFR in the later phase of the eruption, hence a relatively smaller value ($T_c = 0.2$) was used in that study. One should note that not all magnetic field lines satisfying this threshold are summed, only those for which both footpoints lie near the magnetic PIL involved in the flare, and near the subsequent flare ribbons, are included.

In Equation (3), $\Phi_{\rm surrounding}$ indicates the magnetic flux of an external field that suppresses the lifting of an MFR. This term is defined according to the geometry of the field lines relative to the location of the highly twisted field lines (those with $|T_w| > T_c$). In Paper I, two hypotheses were proposed to refine the description of the relevant morphology: $r_m^{\rm o}$, where only the field lines overlying the MFR are considered when calculating the $\Phi_{\rm surrounding}$ term (i.e., $\Phi_{\rm surrounding} = \Phi_{\rm overlying}$), versus $r_m^{\rm o+w}$, where $\Phi_{\rm surrounding}$ is composed of an overlying field and a "wall" field ($\Phi_{\rm surrounding} = \Phi_{\rm overlying} + \Phi_{\rm wall}$), the wall field defined as those field lines that "fence in" the highly twisted region.

To select the overlying field lines and the wall field lines automatically, we project all field lines derived from NLFFF extrapolation onto the photosphere. The overlying field lines are selected as those that intersect the highly twisted field lines along the direction of gravity. Field lines that lie totally beneath the highly twisted field lines were removed from consideration. Wall field lines are those with only one footpoint located near (within 10 Mm) the projection of the highly twisted field lines. The corresponding magnetic flux is then derived by integrating the unsigned normal component of the photospheric magnetic field from the NLFFF extrapolation boundary over the relevant footpoint areas. Next, to test the ability of these newly proposed parameters ($r_m^{\rm o}$ and $r_m^{\rm o+w}$) to distinguish eruptive and confined events, linear discriminant analysis is used (Section 2.4, as was also used in Paper I).

2.4. Linear Discriminant Function Analysis and the Distinguishing Ability of $r_{\rm m}$

The ability of an algorithm to distinguish eruptive from confined flares is verified through linear discriminant function analysis (DA; Leka & Barnes 2003) in this study. The DA is a statistical method that can quantify how exclusive these two groups are based on a distribution of measurements and thus inform the performance of the algorithm.

The DA constructs the discriminant function that can maximize the correct rate of classifying analyzed events into two exclusive groups. In the case of the linear DA, the analyzed events are assumed to be sampled from normally distributed populations. This technique estimates the true probability distribution functions (PDFs) via fitting the samples by Gaussian distributions. The location of the discriminant function is where the two PDFs are equal to each other, i.e., where the two outcomes are predicted to occur with the same probability. With an established discriminant function, we evaluate the classification performance by constructing a classification table, or a contingency table, that tallies the

Table 1
r_m-exception Events for Analysis

Event#[a]	GOES Start Time[b]	GOES Peak Time[c]	GOES End Time[d]	GOES Class[e]
35	2014-10-22T01:16	2014-10-22T01:59	2014-10-22T02:28	M8.7
36	2014-10-22T14:02	2014-10-22T14:28	2014-10-22T14:50	X1.6
37	2014-10-24T21:07	2014-10-24T21:41	2014-10-24T22:13	X3.1

Notes.
[a] The event # is adopted from Paper I.
[b] The start time of the flare according to the GOES catalog.
[c] The peak time of the flare according to the GOES flare catalog.
[d] The end time of the flare according to the GOES flare catalog.
[e] Flare class from the GOES flare catalog.

correct and incorrect classifications. The threshold we use to construct the classification table is the probability when equally observing eruptive events and confined events. We are using Gaussian distributions with equal covariance for representing the PDFs, so we consequently quantify the difference between the two PDFs through metrics such as the Mahalanobis distance. The Mahalanobis distance is a normalized measure of the distance between the sample means, and a large Mahalanobis distance between the two samples indicates that they are likely drawn from different populations.

However, with a single realization using all data points, each data point is used to classify itself, which will tend to underestimate the frequency of incorrect predictions (Hills 1966). Considering the small sample size used in this study (51 analyzed events), which might cause a large bias, we invoke cross-validation to reduce the bias of the results: we remove one data point from the samples and determine the discriminant function based on the remaining data points, and then classify the object according to said discriminant function. For a set with n samples, the procedure is repeated for $n-1$ turns to finally provide an unbiased classification table. With the unbiased classification table, we then compute the corresponding true skill statistic (TSS or the Heidke and Kuiper Skill Score, HKSS; Hanssen & Kuipers 1965) and the correct classification rate by which to judge the classification performance.

Having tested the two hypotheses described in Section 2.3, in Paper I, it was revealed that not only the overlying field lines but also the wall field lines can work to confine a flare's eruptive character. In Paper I, we found that, overall, the r_m scheme could provide a moderate distinguishing ability for the eruptivity of a solar flare when the wall field was included in the overlying-field diagnostic. The resulting classification table constructed with $r_m^{\mathrm{o+w}}$ indicated that six confined events were misclassified as eruptive; among these r_m-exceptional events, three events originated from NOAA AR 12192. We now investigate why.

2.5. Exceptional Events under the $\mathrm{r_m}$ Scheme from NOAA AR 12192

NOAA AR 12192 appeared in 2014 October containing one of the largest sunspots of Cycle 24. It produced more than 140 flares larger than C1.0 class (Bamba et al. 2017). However, these events were atypical because no CME was reported to originate from the core of this AR, only from its periphery (Chen et al. 2015; Thalmann et al. 2015; Panesar et al. 2016). Table 1 lists the relevant flare data as recorded by GOES for the "exceptional" flares, meaning three events from this region which the r_m scheme incorrectly classified as belonging to the "eruptive" population. In addition to these three misclassified events, three other events from AR 12192, one M-class flare and two X-class events, were correctly classified as "confined." The flares listed in Table 1 were also analyzed by Thalmann et al. (2015), where their homologous nature is presented: they are all similar in terms of the integrated properties of flare ribbons, the morphology of the ribbon patterns, and the huge separation between the two early-stage flare ribbons with no evidence of flare-ribbon progression in the lateral direction. Furthermore, Sun et al. (2015) found that AR 12192 had weak nonpotentiality, and Inoue et al. (2016) also concluded that the magnetic configuration prior to the X3.1 flare (event #37) was stable against the kink instability (KI; Hood & Priest 1979; Einaudi & Hoven 1983). The strong overlying magnetic confinement found for the Table 1 targets in these recent studies was found through the simple ratio of magnetic field strengths at differing altitudes (Jing et al. 2015; Sun et al. 2015; Thalmann et al. 2015).

In contrast to these studies, the results in Paper I suggested that the events listed in Table 1 host sufficiently high values of r_m to be classified as eruptive. Figure 1 shows the SDO/AIA observations and the coronal magnetic fields reconstructed from NLFFF extrapolations for these events. Figures 1(a)–(c) show SDO/AIA 94 Å images taken roughly 1 hour prior to the GOES flare start time (that is, the time we have used to construct the NLFFF magnetic field), whereas Figures 1(d)–(e) present the AIA 94 Å observations taken at the GOES peak time listed in Table 1. In each image, one can see the hot coronal loops created through the flares. At the footpoints of these coronal loops, the corresponding emission can be observed in the AIA 1600 Å passband (Figures 1(g)–(i)), implying that these coronal loops trace the magnetic structures where reconnection has occurred. Chen et al. (2015) confirmed that all of the X-class flares from this active region had similar flaring structures as seen in the AIA 94 Å images. We see here, too, that the coronal loops visible in the AIA 94 Å data and the related flare ribbons visible in the 1600 Å images are morphologically similar among these flares, consistent with the homologous character discussed above. The overall twist value is generally less than one-half, consistent with the lack of any clearly visible sigmoidal structure, yet we can recognize inverse-S-shape structures in the SDO/AIA 94 Å images (Figures 1(a)–(c)) and in the reconstructed NLFFF magnetic field (Figures 1(j)–(l)). These structures provide evidence of a flux rope buildup (Green et al. 2011; Green & Kliem 2009; Savcheva et al. 2012), and we suggest that the bright coronal loops indicate the core part of the flares. It should be noted that

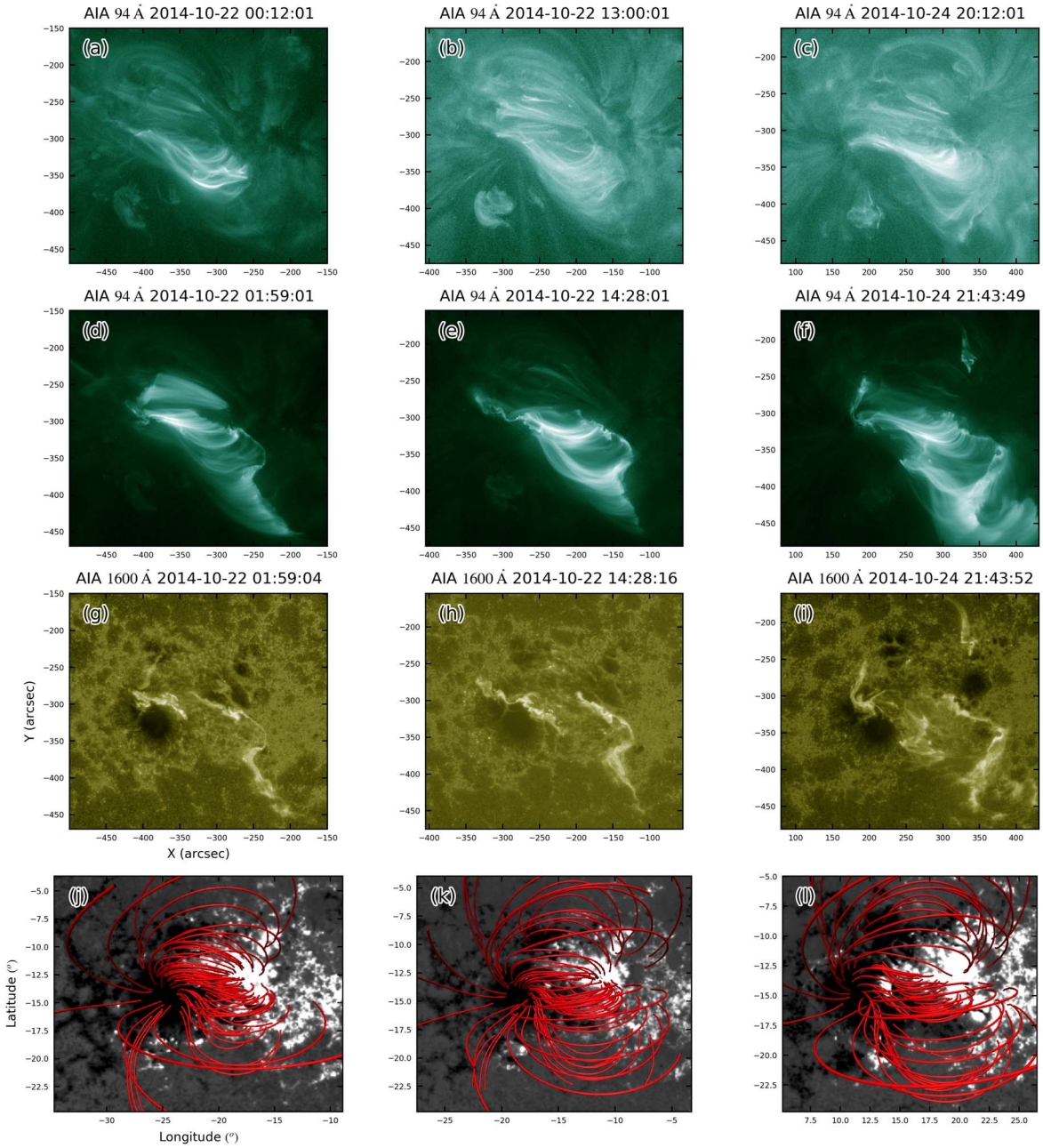

Figure 1. (a)–(c) SDO/AIA 94 observations of AR 12192 taken at a time roughly one hour prior to the GOES flare start time of events #35, #36, and #37, respectively. (d)–(f) The same as in (a)–(c), but taken at the GOES flare peak time. (g)–(i) SDO/AIA 1600 Å observations at the same time as and identical FOV to (d)–(f). (j)–(l) NLFFF extrapolation results of AR 12192 overlaid on SHARP magnetogram data (saturated at ±1500 G). Red lines represent the selected magnetic field lines from the NLFFF extrapolation.

the r_m scheme proposed in Paper I does not in fact require an MFR to be present in the AR, and we suggest that the low-twist profile does not affect the performance of the r_m parameter.

It is worth noting that the low-twist NLFFF magnetic constructions presented here are consistent with those by Inoue et al. (2016) and Jiang et al. (2016) using different NLFFF extrapolation schemes. Veronig & Polanec (2015) argued that there is no observed filament in AR 12192 to indicate an MFR before the X1.6 flare's onset. Prasad et al. (2018) and Jiang et al. (2016) suggested that sheared magnetic arcades actually triggered the onset of the X3.1 flare, implying that an MFR was neither present beforehand nor did one form during the reconnection by the sheared arcade. Sarkar & Srivastava (2018) also noted the absence of photospheric flux cancellation under the postflare loops among the confined events, which implies there would be no footpoint reconnection along the PIL available to form an MFR.

Regarding the magnetic field above the core region, we have calculated the horizontal component of the magnetic field directly above the PIL at the height of 42 Mm to directly compare with the model used in Sun et al. (2015), and we find comparable horizontal field strengths. This implies that the cause(s) of the incorrect classification by r_m is not due to problems with the NLFFF model employed here.

3. Analysis

In this section, we explore factors that may have led to the incorrect eruptive-potential diagnosis of AR 12192 with the r_m parameter. Two hypotheses are presented here for testing: first, that the ratio of magnetic fluxes used as the approximation for the force balance (Equation (3)) could be better estimated by the ratio of other physical quantities. Second, we postulate that using the threshold $\Phi_{|T_w|\geqslant 0.2}$ cannot adequately approximate $\Phi_{\rm reconnect}$ to which an MFR will contribute. In this section, we motivate and test these hypotheses.

3.1. Testing Hypothesis #1: The r_τ Parameter and r_κ Parameter

As described above, r_m is defined as the ratio of the magnetic flux of the footpoints of different bundles of field lines (see Equation (3)). Here we investigate whether the success of the eruptive assignment can be improved by replacing the magnetic flux with other physical quantities.

The magnetic twist flux density (τ) was introduced by Kusano et al. (2020):

$$\tau = T_w |B_z|, \tag{4}$$

where B_z is the same radial (normal) magnetic field component used to calculate total flux (here we use the lower boundary of the NLFFF extrapolation, for which B_z is held fixed during relaxation), and T_w is the wind number (Equation (1)). Based on Equation (4), the "magnetic twist flux" (Φ_τ) is therefore computed as

$$\Phi_\tau = \int \tau \, dS, \tag{5}$$

where dS is a finite element in the surface integral on the photosphere. Φ_τ is used to estimate κ, a critical parameter used to evaluate the double-arc instability (DAI; Ishiguro & Kusano 2017). DAI is proposed to explain the onset of a double-arc coronal loop formed through tether-cutting reconnection (Moore et al. 2001), hence Φ_τ can be considered a measure of the capability of an AR to trigger an energetic event. Replacing the magnetic flux (Φ) in Equation (6) with the magnetic twist flux, we define a new parameter:

$$r_\tau = \frac{\Phi_{\tau\ T_w \geqslant T_c}}{\Phi_{\tau\ T_w \geqslant T_c} + \Phi_{\tau\ \rm surrounding}}, \tag{6}$$

where the Φ_τ relies on the field-line twist (T_w), thus we impose the threshold $T_c = 0.2$ and include only those footpoints for magnetic field lines with $|T_w| \geqslant T_c$ where $|T_w| \geqslant 0.2$ for Φ_τ; no such limit is used for $\Phi_{\tau\ \rm surrounding}$. According to the theoretical definition of κ, the area integral for calculating Φ_τ is taken over the region where the tether-cutting reconnection has extended ($S_{\rm rec}$). A magnetogram cannot provide information on the location and extent of $S_{\rm rec}$ independently, hence its implementation has varied: Muhamad et al. (2018) approximated $S_{\rm rec}$ as areas with associated field lines that have $T_w > 0.5$. Kusano et al. (2020) assumed that $S_{\rm rec}$ was a circular region centered at points along a PIL, calculating the corresponding κ value along the full PIL to find the location most unstable against DAI. Because our objective is to explore whether using other physical quantities can improve the assignment of eruptive or confined across all events, we vary only one thing at a time and consequently use the same area integral as in Paper I, specifically the area with $|T_w| \geqslant 0.2$. Similarly, when estimating $\Phi_{\tau\ \rm overlying}$ and $\Phi_{\tau\ \rm wall}$, we apply identical procedures for selecting those field lines, summarized as:

1. *Highly twisted field*: field lines where $T_w \geqslant 0.2$; closed field lines lying near that PIL involved in the flare and hence near, but not necessarily cospatial with, the flare ribbons.
2. *Overlying field*: closed field lines lying above the highly twisted region; excludes highly twisted field.
3. *Wall field*: field lines with one footpoint near the highly twisted field ($\leqslant$10 Mm) and the other footpoint away from it, but still must be closed; excludes highly twisted field.

To avoid large uncertainties, we only consider data where the radial component of the magnetic field strength exceeds 250 G, a somewhat conservative but otherwise arbitrary threshold above which the derived magnetic flux was not sensitive.

As a further refinement, consider that the original definition of κ was given by the ratio of magnetic twist flux (Φ_τ) over the magnetic flux (Φ). We extend this to

$$r_\kappa = \frac{\Phi_{\tau\ T_w \geqslant T_c}}{\Phi_{T_w \geqslant T_c} + \Phi_{\rm surrounding}}, \tag{7}$$

which differs from Equation (6) in that the denominator in Equation (7) is Φ instead of Φ_τ. The parameters κ and r_κ are formulated from the concept that the magnetic flux (Φ) rather than the magnetic twist flux (Φ_τ) should work to suppress eruption.

Thus, we now have three different parameters, r_m, r_τ, and r_κ, all of which assume that field lines with large T_w can approximate the MFR's field lines. We group these parameters as the *r*-scheme for estimating the likelihood of a flare being an eruptive flare. One should note that all parameters are based on the ratio of the driving force to the suppressing force, as estimated using flux (or twist flux) corresponding to twisted field lines (driving) in the numerator and flux (or twist flux) corresponding to field lines that could be involved with suppression in the denominator. We highlight the differences in the numerator and denominator sources of footpoint flux here:

1. $r_m^{\rm o}$: ratio of magnetic flux; numerator: field lines where $|T_w| \geqslant 0.2$; denominator: overlying field only (proposed by Paper I as $r_m^{\rm h1}$).
2. $r_m^{\rm o+w}$: ratio of magnetic flux; numerator: field lines where $|T_w| \geqslant 0.2$; denominator: overlying field and wall field (proposed by Paper I as $r_m^{\rm h2}$).
3. $r_\tau^{\rm o}$: ratio of magnetic twist flux; numerator: field lines where $|T_w| \geqslant 0.2$; denominator: overlying field only.
4. $r_\tau^{\rm o+w}$: ratio of magnetic twist flux; numerator: field lines where $|T_w| \geqslant 0.2$; denominator: overlying field and wall field.
5. $r_\kappa^{\rm o}$: ratio of magnetic twist flux over magnetic flux; numerator: field lines where $|T_w| \geqslant 0.2$; denominator: overlying field only.
6. $r_\kappa^{\rm o+w}$: ratio of magnetic twist flux over magnetic flux; numerator: field lines where $|T_w| \geqslant 0.2$; denominator: overlying field and wall field.

Table 2
Estimations Related to r_τ and r_κ

Event#	$\Phi_{T_w \geqslant T_c}$ ±0.6%[a] (10^{20} Mx)	$\Phi_{\tau\ T_w \geqslant T_c}$ ±5.3% (10^{20} Mx)	$\Phi_{\rm overlying}$ ±9.8% (10^{20} Mx)	$\Phi_{\tau\ \rm overlying}$ ±28.6% (10^{20} Mx)	$\Phi_{\rm wall}$ ±1.3% (10^{20} Mx)	$\Phi_{\tau\ \rm wall}$ ±10.2% (10^{20} Mx)	r_τ^{o} [b] ±3.3%	r_τ^{o+w} [c] ±6.7%	r_κ^{o} [d] ±3.1%	r_κ^{o+w} [e] ±5.1%
1	29.52	12.97	6.45	1.25	51.29	4.03	0.91	0.71	0.36	0.15
2	36.54	17.49	8.21	1.16	93.55	9.81	0.94	0.61	0.39	0.13
3	17.93	6.09	40.15	2.51	25.65	3.31	0.71	0.51	0.10	0.07
4	7.27	2.58	9.31	1.16	11.23	0.96	0.69	0.55	0.16	0.09
5	18.77	6.97	16.16	1.60	24.53	2.21	0.81	0.65	0.20	0.12
6	25.90	9.34	12.52	1.25	32.70	2.21	0.88	0.73	0.24	0.13
7	13.80	4.93	5.61	0.43	16.74	0.59	0.92	0.83	0.25	0.14
8	15.53	6.76	6.57	0.41	16.19	0.52	0.94	0.88	0.31	0.18
9	12.48	5.85	13.48	1.28	17.50	0.61	0.82	0.76	0.23	0.13
10	2.91	0.93	17.32	0.93	3.78	0.45	0.50	0.40	0.05	0.04
11	136.77	52.15	144.36	10.72	17.88	1.09	0.83	0.82	0.19	0.17
12	124.61	47.73	144.58	11.00	24.63	1.64	0.81	0.79	0.18	0.16
13	122.62	42.51	107.94	9.59	12.76	0.61	0.82	0.81	0.18	0.17
14	37.66	13.25	52.18	3.20	27.03	1.97	0.81	0.72	0.15	0.11
15	6.31	3.25	18.58	2.74	36.44	3.17	0.54	0.35	0.13	0.05
16	4.80	1.35	6.91	0.74	15.36	0.93	0.65	0.45	0.12	0.05
17	4.61	1.66	21.47	4.86	65.38	7.52	0.25	0.12	0.06	0.02
18	4.24	1.62	24.13	5.94	68.58	7.99	0.21	0.10	0.06	0.02
19	67.46	24.87	75.98	7.61	77.16	8.08	0.77	0.61	0.17	0.11
20	5.51	1.38	5.22	0.33	13.45	1.21	0.81	0.47	0.13	0.06
21	6.42	3.22	7.16	0.71	14.06	1.15	0.82	0.63	0.24	0.12
22	7.45	3.12	12.13	1.21	22.97	1.97	0.72	0.50	0.16	0.07
23	5.67	2.17	14.17	0.78	9.54	0.87	0.74	0.57	0.11	0.07
24	10.74	4.61	28.55	3.05	59.92	3.66	0.60	0.41	0.12	0.05
25	12.31	3.16	68.21	4.55	12.64	1.00	0.41	0.36	0.04	0.03
26	9.88	5.13	25.97	2.08	25.87	3.20	0.71	0.49	0.14	0.08
27	20.83	6.60	15.55	1.37	43.14	3.95	0.83	0.55	0.18	0.08
28	10.87	4.91	62.11	4.46	48.35	4.19	0.52	0.36	0.07	0.04
29	0	0	0	0	0	0	0	0	0	0
30	33.00	15.24	31.23	2.81	61.51	5.62	0.84	0.64	0.24	0.12
31	11.57	4.34	4.49	0.35	3.17	0.06	0.93	0.91	0.27	0.23
32	5.33	1.40	15.32	1.15	13.09	0.99	0.55	0.40	0.07	0.04
33	48.11	14.27	67.60	6.94	15.24	1.21	0.67	0.64	0.12	0.11
34	35.88	10.86	35.54	3.45	61.11	4.06	0.76	0.59	0.15	0.08
35	121.10	42.14	137.76	16.54	185.04	12.96	0.72	0.59	0.16	0.09
36	158.06	52.17	132.80	15.00	202.44	12.45	0.78	0.66	0.18	0.11
37	111.71	32.82	98.00	13.44	187.26	17.95	0.71	0.51	0.16	0.08
38	40.56	13.49	89.32	15.93	186.15	19.89	0.46	0.27	0.10	0.04
39	35.74	10.77	44.45	5.79	197.15	17.95	0.65	0.31	0.13	0.04
40	43.25	15.51	52.51	5.52	239.52	21.73	0.74	0.36	0.16	0.05
41	42.54	15.88	38.69	3.94	29.68	1.71	0.80	0.74	0.20	0.14
42	5.55	1.46	29.71	2.77	21.26	1.52	0.34	0.25	0.04	0.03
43	67.96	21.12	21.99	2.37	52.87	5.14	0.90	0.74	0.23	0.15
44	47.47	18.08	33.83	2.93	19.79	2.71	0.86	0.76	0.22	0.18
45	66.90	22.17	81.90	8.26	45.94	4.94	0.73	0.63	0.15	0.11
46	5.16	1.88	0.56	0.03	11.31	0.58	0.99	0.76	0.33	0.11
47	9.66	4.28	14.35	2.32	63.24	12.71	0.65	0.22	0.18	0.05
48	71.05	32.00	65.79	6.72	20.47	1.48	0.83	0.80	0.23	0.20
49	48.55	15.41	73.60	7.59	31.12	2.73	0.67	0.60	0.13	0.10
50	0.75	0.34	12.59	0.82	11.73	1.48	0.29	0.13	0.03	0.01
51	5.66	2.13	22.75	2.67	46.91	4.94	0.44	0.22	0.08	0.03

Notes.
[a] The uncertainties are presented assuming all magnetic fluxes estimated in event #1 are representative.
[b] r_τ calculated based on hypothesis 1 ($\Phi_{\tau\ \rm surrounding} = \Phi_{\tau\ \rm overlying}$).
[c] r_τ calculated based on hypothesis 2 ($\Phi_{\tau\ \rm surrounding} = \Phi_{\tau\ \rm overlying} + \Phi_{\tau\ \rm wall}$).
[d] r_κ calculated based on hypothesis 1 ($\Phi_{\rm surrounding} = \Phi_{\rm overlying}$).
[e] r_κ calculated based on hypothesis 2 ($\Phi_{\rm surrounding} = \Phi_{\rm overlying} + \Phi_{\rm wall}$).

The quantities used to calculate Equations (6) and (7), and the resulting $r_\tau^{\rm o}$, $r_\tau^{\rm o+w}$, $r_\kappa^{\rm o}$ and $r_\kappa^{\rm o+w}$, are presented in Table 2, with the corresponding uncertainties quoted in the table header (see Appendix C for the estimation of uncertainty). The deduced uncertainties of the Φ results are generally less than 10%, although those for some Φ_τ parameters are larger,

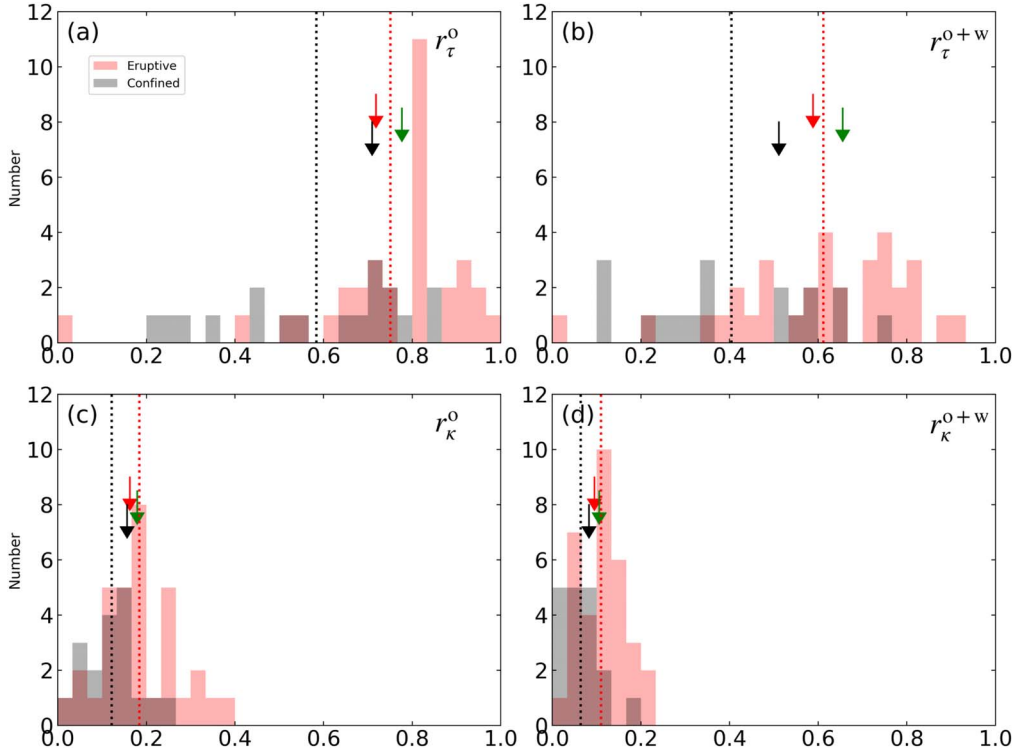

Figure 2. Histograms of (a) $r_\tau^{\rm o}$, (b) $r_\tau^{\rm o+w}$, (c) $r_\kappa^{\rm o}$, and (d) $r_\kappa^{\rm o+w}$ for eruptive events (shaded red) and confined events (shaded gray). Red (black) vertical dashed lines indicate the mean value of the variables for eruptive (confined) events. The arrows colored red, green, and black indicate the value that events #35, #36, and #37 host, respectively.

reaching just over 25%. We suggest that this is due to the propagation of errors through the NLFFF extrapolation, influencing those quantities involving the twist number (which is computed using the NLFFF construction). The zero values that appear in event #29 are due to there being no field lines in the flare-ribbon area that satisfy the threshold ($|T_w| \geqslant 0.2$); hence, all values are assigned zero. The distributions of $r_\tau^{\rm o}$, $r_\tau^{\rm o+w}$, $r_\kappa^{\rm o}$, and $r_\kappa^{\rm o+w}$ are shown in Figure 2. We find that the average value of the eruptive events is always greater than the confined events in each parameter (which are denoted by the red and black dashed lines in Figure 2, respectively). Moreover, the values of r_τ are overall higher than r_κ, owing to the smaller denominator (see Equation (6)): the coronal field lines generally have $|T_w| < 1$, hence, in general, $\Phi > \Phi_\tau$.

With the resulting $r_\tau^{\rm o}$, $r_\tau^{\rm o+w}$, $r_\kappa^{\rm o}$, and $r_\kappa^{\rm o+w}$ across all 51 events, we test the ability of these variables to distinguish between eruptive and confined through the application of linear DA, as was used in Paper I (see Section 2.4). The statistical metrics used to judge the discrimination of these variables are summarized in Table 3. The results from these statistical metrics demonstrate that the eruptivity can be classified using the parameters proposed here; however, as acknowledged in Paper I, a large overlap of the two distributions implies that still-unknown physical mechanisms are involved in triggering energetic events.

For each of the DA-produced metrics presented in Table 3, we provide uncertainties derived by Monte Carlo and 100-draw bootstrap algorithms. The Monte Carlo algorithm measures the uncertainties arising from the uncertainties in the observations, while the bootstrap measures the uncertainties generated by the sampling process (see Appendix C for further details on these two techniques). A comparison of all metrics and their uncertainties are presented in Figure 3 (the q parameters are discussed in Section 3.2). The rather large uncertainties in r_τ and r_κ imply that we have too small a sample size in this study to accurately estimate the true distributions of each population.

According to the metrics presented in Table 3 and Figure 3, we find that $r_\tau^{\rm o+w}$ show larger values than other parameters: for example, the higher probability that two samples are from different populations suggests that using $r_\tau^{\rm o+w}$ may better distinguish the eruptive from confined populations, although the value of the probability is still insufficient to definitively state that the samples are from distinct populations. The larger Mahalanobis distance, correct rate (RC), and true skill statistic (TSS; computed as with RC using a probability threshold of 0.5) all indicate that eruptive and confined events are more separated by the $r_\tau^{\rm o+w}$ measure. In spite of the performance of $r_\tau^{\rm o+w}$ being ostensibly superior to $r_m^{\rm o+w}$, this does not guarantee that the latter is the best-performing variable, due to the small sample size and the resulting large uncertainties (see Figure 3). In general, compared to the $r_m^{\rm o}$ and $r_m^{\rm o+w}$ parameters proposed in Paper I, all parameters listed in Table 2 remain at a "moderate" level in evaluating the eruptivity of the flares. Of note, the $n-1$ cross-validation results show that the three targeted events (event #35, #36, and #37) are still classified as "eruptive" even with the newly refined parameters. In other words, the values of the newly proposed parameters for these three events do not decrease compared to the other events, and according to the DA, approximating the force balance by other physical quantities, such as Φ_τ, cannot fix the classification errors in these three cases.

3.2. Testing Hypothesis # 2 with the q-schemes: $q_{\rm m}$, q_τ, and q_κ

Here we test the second hypothesis, "$\Phi_{|T_w|\geqslant 0.2}$ cannot adequately approximate the $\Phi_{\rm reconnection}$ that is contributed by

Table 3
DA Results (with $n-1$ Cross-validation) of the Parameters in the r-scheme

Parameter	Method	Statistical Quantities			
		Probability[a]	MD[b]	CR[c]	TSS
r_m^{o} [d]	Original	94%	0.63	0.65	0.15
	Monte Carlo	93.9% ± 0.4	0.63 ± 0.02	0.66 ± 0.01	0.17 ± 0.02
	Bootstrap	84.5 ± 17.4%	0.59 ± 0.41	0.67 ± 0.07	0.14 ± 0.18
r_m^{o+w} [e]	Original	96.9%	0.85	0.73	0.37
	Monte Carlo	96.9 ± 0.2%	0.85 ± 0.02	0.73 ± 0.01	0.38 ± 0.02
	Bootstrap	89.8 ± 12.7%	0.78 ± 0.57	0.69 ± 0.07	0.20 ± 0.19
r_τ^{o}	Original	95.1%	0.7	0.71	0.24
	Monte Carlo	87.1 ± 21.0%	0.74 ± 0.41	0.70 ± 0.04	0.21 ± 0.13
	Bootstrap	86.0 ± 18.3%	0.75 ± 0.58	0.69 ± 0.07	0.18 ± 0.17
r_τ^{o+w}	Original	98.2%	1.03	0.76	0.43
	Monte Carlo	91.1 ± 19.1%	0.98 ± 0.47	0.71 ± 0.04	0.29 ± 0.15
	Bootstrap	93.0 ± 10.4%	0.98 ± 0.61	0.72 ± 0.07	0.27 ± 0.20
r_κ^{o}	Original	93.1%	0.59	0.68	0.21
	Monte Carlo	83.5 ± 21.3%	0.52 ± 0.26	0.66 ± 0.04	0.09 ± 0.12
	Bootstrap	84.9 ± 16.7%	0.57 ± 0.35	0.66 ± 0.07	0.10 ± 0.17
r_κ^{o+w}	Original	96.6%	0.82	0.67	0.28
	Monte Carlo	79.6 ± 25.0%	0.52 ± 0.33	0.66 ± 0.04	0.11 ± 0.16
	Bootstrap	89.7 ± 12.9%	0.76 ± 0.49	0.68 ± 0.06	0.18 ± 0.18

Notes.
[a] Probability that the samples arise from different populations.
[b] Mahalanobis distance for the sample PDFs.
[c] Correct rate of the classification table.
[d] The same as the r_m^{h1} from Paper I.
[e] The same as the r_m^{h2} from Paper I.

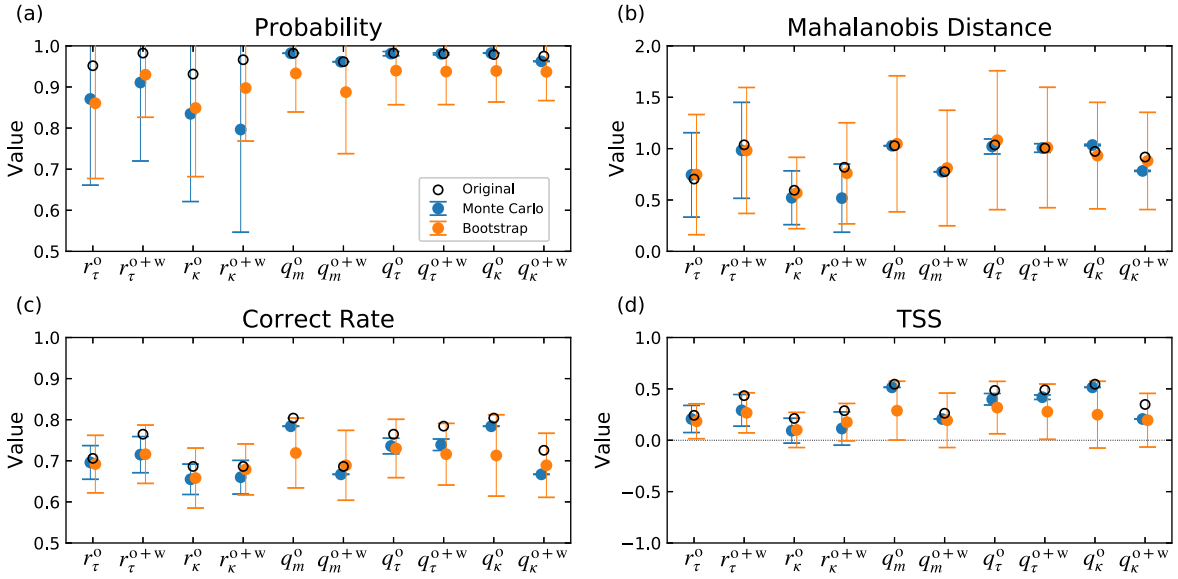

Figure 3. The comparison of the resulting DA metrics for the r-scheme (r_τ^{o}, r_τ^{o+w}, r_κ^{o}, and r_κ^{o+w}) and q-scheme (q_m^{o}, q_m^{o+w}, q_τ^{o}, q_τ^{o+w}, q_κ^{o}, and q_κ^{o+w}). The metrics are (a) the probability that the two groups are sampled from two distinct populations, (b) Mahalanobis distance, (c) correct rate, and (d) TSS. The unfilled black circles indicate the value yielded through the $n-1$ cross-validation. The data points and the associated error bars colored in blue (orange) stand for the estimations yielded by the Monte Carlo algorithm (bootstrap method). A horizontal dashed line in (d) divides the space of positive and negative skills for the classification.

an MFR." We have shown that modifying the scheme of r_m to use the ratio of other physical quantities (i.e., r_τ and r_κ) still resulted in the three targeted events being incorrectly classified as eruptive events. The problem now narrows to how to verify whether the threshold of $|T_w| \geqslant 0.2$ is a proper criterion for these targeted events. To do this, we test the option of instead using the flare-ribbon emission area, which is regarded to be a more direct approximation of the reconnected magnetic flux. It is widely regarded that flare ribbons are strongly related to magnetic reconnection, as it is the precipitation of the energetic

particles released by magnetic reconnection which is believed to cause emission in the Hα line center and the 1600 bandpass (Forbes 2000; Qiu et al. 2012). The area "swept" by flare ribbons has a quantitative relationship to the magnetic reconnection progress (Priest & Forbes 2002; Qiu et al. 2012). According to the well-known CSHKP "standard flare" model, the flare-ribbon area corresponds to where newly reconnected field lines anchor on the solar surface. Based on the 3D version of the CSHKP model, Kazachenko et al. (2017) showed the relation between peak X-ray flux and the flare-ribbon area's magnetic flux, demonstrating that the amount of energy released by magnetic reconnection can be directly deduced from the measurement of the flare-ribbon area and its associated magnetic flux. Tschernitz et al. (2018) found that for a given GOES class, there is no significant difference between the eruptive and confined events with regard to the total reconnected magnetic flux involved at the flare onset (inferred from the flare ribbons), whereas the mean magnetic flux density swept by the ribbons was significantly larger in the confined events. This result implies that confined events could tend to occur closer to the flux-weighted center of an AR where a substantial overlying field is expected to exist. Overall, Tschernitz et al. (2018) have demonstrated that flare-ribbon information could serve as a useful indicator of the likelihood of CME eruptivity.

By using the flare-ribbon-defined magnetic flux as a representation of the reconnected magnetic flux, we propose the q-scheme, which is a modified version of the aforementioned r-scheme. The q-scheme includes the parameters defined as follows:

$$q_m = \frac{\Phi_{\rm Ribbon}}{\Phi_{\rm Ribbon} + \Phi_{\rm surrounding,R}}, \tag{8}$$

$$q_\tau = \frac{\Phi_{\tau\ \rm Ribbon}}{\Phi_{\tau\ \rm Ribbon} + \Phi_{\tau\ \rm surrounding,R}}, \tag{9}$$

$$q_\kappa = \frac{\Phi_{\tau\ \rm Ribbon}}{\Phi_{\rm Ribbon} + \Phi_{\rm surrounding,R}}, \tag{10}$$

where $\Phi_{\rm surrounding,R}$ indicates that the surrounding field is defined based on the flare-ribbon area. We now have six new variables:

1. $q_m^{\rm o}$: ratio of magnetic flux; numerator: ribbon-associated-magnetic field; denominator: overlying field only.
2. $q_m^{\rm o+w}$: ratio of magnetic flux; numerator: ribbon-associated-magnetic field; denominator: overlying field and wall field.
3. $q_\tau^{\rm o}$: ratio of magnetic twist flux; numerator: ribbon-associated-magnetic field; denominator: overlying field only.
4. $q_\tau^{\rm o+w}$: ratio of magnetic twist flux; numerator: ribbon-associated-magnetic field; denominator: overlying field and wall field.
5. $q_\kappa^{\rm o}$: ratio of magnetic twist flux over magnetic flux; numerator: ribbon-associated-magnetic field; denominator: overlying field only.
6. $q_\kappa^{\rm o+w}$: ratio of magnetic twist flux over magnetic flux; numerator: ribbon-associated-magnetic field; denominator: overlying field and wall field.

It is important to note that the q-scheme approximates the MFR's footpoints by the area covered by flare ribbons as seen in the 1600 Å wavelengths, rather than the area of high field-line twist number as in the r-scheme. According to the 3D version of the CSHKP model, during the flare-eruption process, the newly reconnected field lines in the immediate vicinity of a PIL are progressively incorporated into the reconnection, hence the brightening patterns gradually progress in space during the flare. We define as the flare-ribbon area all pixels that increased in brightness above a specified intensity threshold between the flare start time and end times as listed in the GOES catalog. The sensitivity of our analysis to the brightness threshold is discussed in Appendix D.

However, prior to constructing the mask, we remove the saturated pixels in the AIA 1600 Å channel images due to overexposure throughout the flaring period. We first remap the 24 s cadence 1600 Å AIA data sequence from the CCD coordinates into the CEA projections to match the HMI SHARP data used for the NLFFF extrapolation. We then follow the procedures described in Kazachenko et al. (2017) but adjust the value of the threshold for identifying the saturated pixels (to $I_{\rm sat} = 9000\,{\rm counts\,s^{-1}}$). The temporal interpolation is performed over the time range from the GOES-listed start time to the end time.

Figure 4 shows the saturation-corrected image sequences for event #36. Before the saturation (Figures 4 (a) and (b)), the technique does not modify any pixel. During the phase of greatest saturation (Figures 4(c) and (d)), only saturated pixels and their surroundings are replaced with the interpolated values. Images taken when the saturation just finished (Figures 4(e) and (f)) show minimal changes to the major characteristics of the flare ribbons. The saturation-correction method is applied on each frame throughout the flaring phase for every event under analysis, providing automatically corrected AIA observation sequences for the 51 events. This approach is an image-processing technique with no consideration as to the physical effect on the chromosphere; we nevertheless use this approach because Kazachenko et al. (2017) demonstrated that this technique can give a reasonable accumulated light curve.

Finally, with these saturation-removed image sequences, we make a cumulative mask to preserve all pixels that brightened above the intensity threshold between the GOES start time and end time. We demonstrate in Figure 5 the construction of the flare-ribbon masks: (a) identify the pixels exceeding the intensity threshold, and shift the mask to be coaligned with the lower boundary magnetogram used in NLFFF according to solar differential rotation, (b) degrade the spatial resolution to match the magnetogram that serves as the lower boundary for the NLFFF extrapolation (see Appendix B), (c) remove small gaps appearing in the mask, smooth the boundaries, and assign regions with unique labels (partitions) using the `closing` function of the `skimage` module in Python (van der Walt et al. 2014). and (d) after partitioning, small patches with area less than 60 pixels (about $1.8 \times 10^{18}\,{\rm cm^2}$) are removed for a "sanitized" flare-ribbon mask. We perform this sanitizing process because field lines rooted in low-signal magnetic regions (noise-dominated areas) will bring considerable uncertainty to the determination of overlying and wall fields. We recognize the possibility that the process to sanitize the image may remove some important features. For instance, in Figure 5, the small gap in the negative-polarity side of the flare ribbons is removed by this technique, although it is a real feature of a polarity intrusion and not noise (Veronig & Polanec 2015). However, the technique we describe is

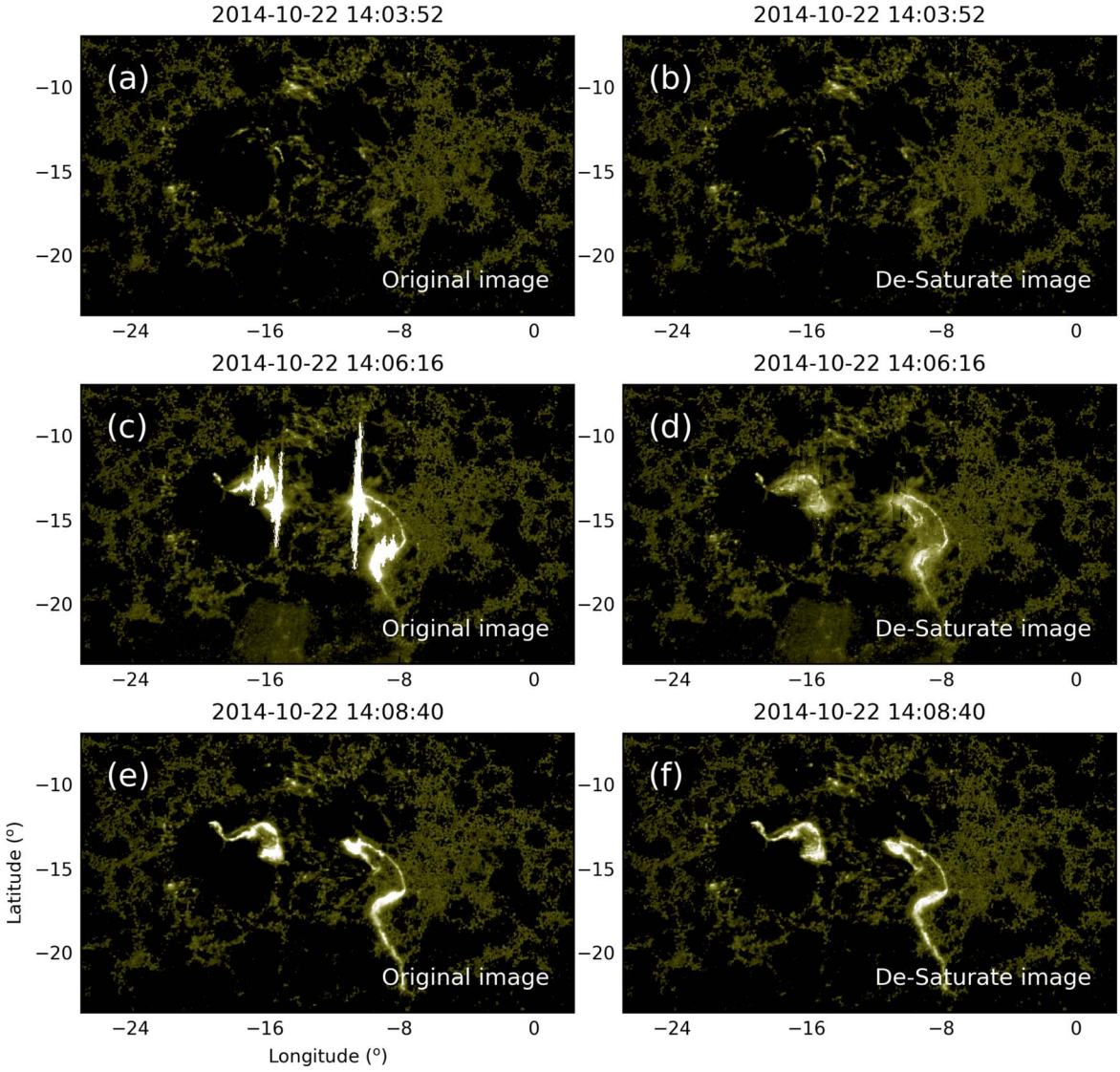

Figure 4. SDO/AIA 1600 Å images remapped into CEA projections show the evolution of the flare ribbons on 2014 October 22 (event #36 in Table 1). Left column: original AIA image sequence. Right column: images after applying saturation correction. (a)–(b) Snapshots of the flare ribbons at the initial phase, with no saturated pixels detected. (c)–(d) Snapshots of the flare ribbons when the largest number of saturated pixels are detected. (e)–(f) Snapshots of the flare ribbons during the gradual decay phase; again, no saturated pixels are detected.

repeatable and the resulting masks are objective, with hopefully a minimal number of feature-removal cases as described above. We superimpose the processed mask on the lower boundary B_z of the NLFFF model for analysis.

We assume that field lines from footpoints associated with post-reconnection heating still have a direct relation to field lines in a model computed prior to any reconnection, justifying the use of a pre-event NLFFF model in conjunction with the flare-ribbon mask to identify field lines of interest. In Figure 5(e), the selected flare-ribbon field lines are presented, specifically only those field lines with both footpoints anchored cospatially with flare ribbons.

We include only these field lines in the analysis in order to approximate the reconnect-imminent field because we assume that an MFR that formed before event-related reconnection will have conjugate footpoints located in opposite polarities but in the vicinity of the flare ribbons. The corresponding overlying and wall field lines are consequently defined according to the description in Section 2.3 (see Figure 5(f)). To summarize the definitions which will be applied in the q-scheme analysis:

1. *Flare-ribbon-related field*: field lines with both field lines anchoring in the flare ribbons; closed field lines; no requirement on T_w.
2. *Overlying field*: field lines lying above the flare-ribbon-related field; closed field lines; excludes flare-ribbon-related field; no requirement on T_w.
3. *Wall field*: field lines with one footpoint $\leqslant$10 Mm from the flare-ribbon-related field, the other footpoint $\gg$ 10 Mm from any flare-ribbon-related field; closed field lines; excludes flare-ribbon-related field; no requirement on T_w.

Of note, although the highly twisted field used in the r-scheme also includes the information on flare ribbons, the major difference between these two schemes is that there is no restriction on T_w for the flare-ribbon-related field. Moreover, the footpoints of flare-ribbon-related field lines are coincident

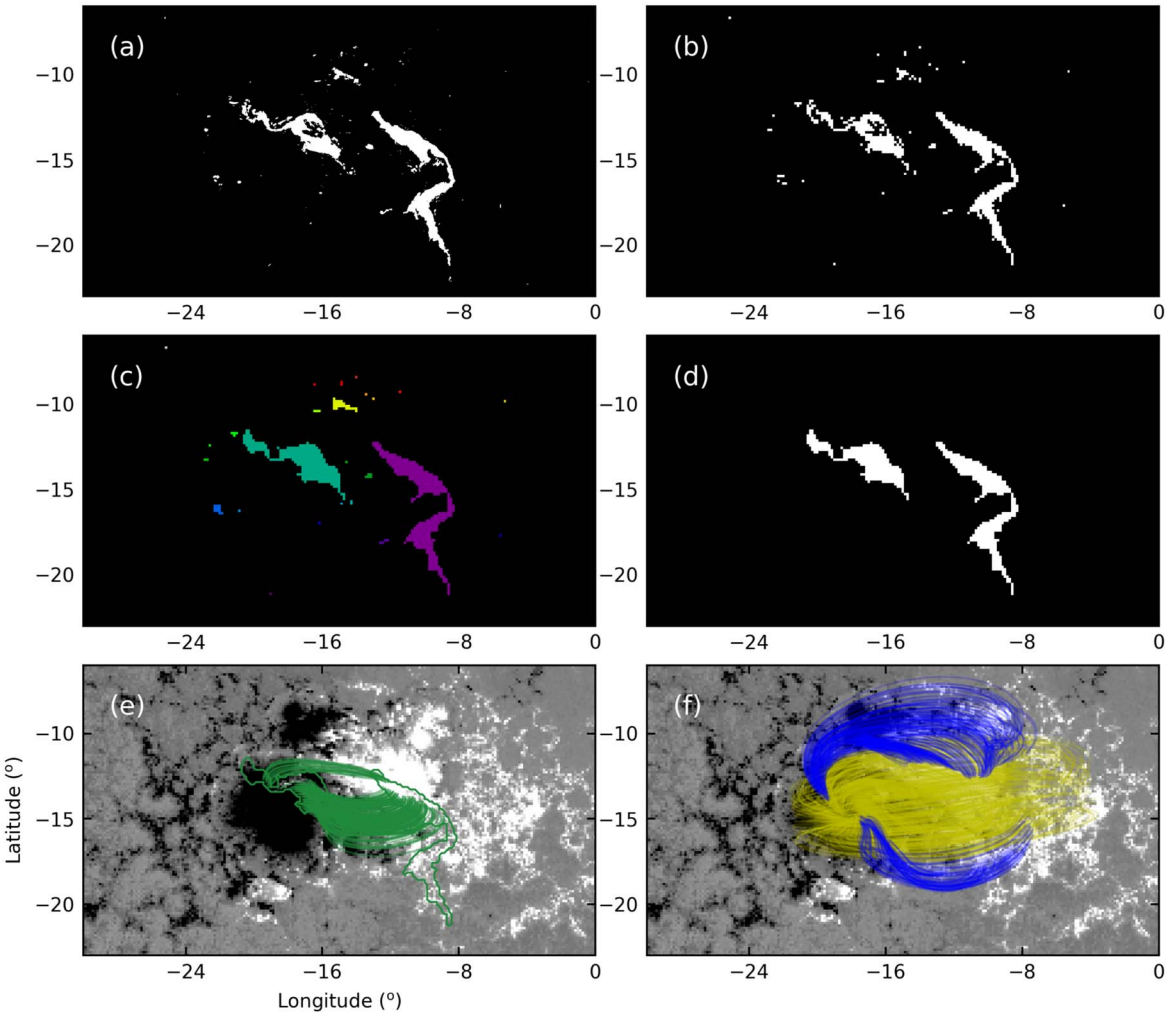

Figure 5. Deriving the $\Phi_{\rm Ribbon}$, $\Phi_{\rm overlying,\ R}$, and $\Phi_{\rm wall,\ R}$, demonstrated on event #36. (a) Original flare-ribbon mask constructed from the de-saturated and remapped SDO/AIA 1600 observations. See text for details. (b) the flare-ribbon mask from (a) now degraded to the spatial resolution consistent with the lower boundary used in the NLFFF extrapolation; (c) the labeling result of the flare-ribbon mask; (d) sanitized flare-ribbon mask with only the main body of the flare ribbons retained; (e) field lines (green) which have both footpoints anchored in the proposed flare-ribbon mask (indicated by green contours) (f) field lines in the overlying field (yellow) and wall field (blue). All the maps are shown in the CEA projection.

with the flare ribbons, whereas the highly twisted field lines are roughly falling into the area in which ribbons appear. As both schemes involve the information of flare ribbons, there are some field lines selected by both the *r*- and *q*-schemes to represent the MFR.

After determining the specific field lines targeted for analysis, the magnetic flux and magnetic twist flux are calculated with surface integration over the targeted footpoint pixels. The resulting q_m, q_τ, and q_κ are then inferred according to Equations (8)–(10), respectively. The quantities used to derive q_m, q_τ, and q_κ are summarized in Table 4, and the associated uncertainties are quoted in the header as derived following the approaches described in Appendix C. Surprisingly, even though the identical technique is performed here, the error of each parameter is significantly smaller compared to that found for the *r*-scheme. We conclude that fluxes from the surface integral over the flare-ribbon area are not sensitive to the observational uncertainties. Of note, in event #50, the value of the flare-ribbon flux is zero as we failed to identify any field lines that have both footpoints anchored within the flare ribbons. The values of the *q* parameters that have similar "null-set" issues are also assigned to zero.

The distributions of all the parameters in the *q*-scheme are presented in Figure 6 for the two populations, eruptive events and confined events. It appears that the eruptive events in general have greater values among all the *q*-scheme parameters. The mean values of the two populations indicate that the eruptive group always presents higher values than the confined group across all *q*-scheme parameters. Even though q_κ now occupies a rather narrow parameter space, one can see that the two distributions still peak at distinct values, with the eruptive population exceeding the confined one, on average. The results imply a tendency that across each variation in the algorithm, the suppression term tends to be weaker for the eruptive events. The distributions also reveal that the values for q_κ (which contains $q_\kappa^{\rm o}$ and $q_\kappa^{\rm o+w}$) are generally smaller than those for other parameters, due to the numerator (Φ_τ) being generally smaller than the denominator (Φ). The values of the target events for each *q*-parameter are indicated in Figure 6. We find that compared to their values in the *r*-scheme parameters (Figure 2), the target events' *q*-scheme values have decreased overall and are now correctly classified as " confined" by most of the *q*-based parameters (see Table 7).

Table 4
Estimations Related to q_m, q_τ, and q_κ

Event#	$\Phi_{\rm Ribbon}$ $\pm0.1\%$ (10^{20}Mx)	$\Phi_{\tau\ \rm Ribbon}$ $\pm2.2\%$ (10^{20} Mx)	$\Phi_{\rm overlying,\ R}$ $\pm0.1\%$ (10^{20} Mx)	$\Phi_{\tau\ \rm overlying,\ R}$ $\pm0.8\%$ (10^{20} Mx)	$\Phi_{\rm wall,\ R}$ $\pm0.1\%$ (10^{20} Mx)	$\Phi_{\tau\ \rm wall,\ R}$ $\pm3.8\%$ (10^{20} Mx)	$q_m^{\rm o}$ [a] $\pm0.1\%$	$q_m^{\rm o+w}$ [b] $\pm0.1\%$	$q_\tau^{\rm o}$ [c] $\pm1.4\%$	$q_\tau^{\rm o+w}$ [d] $\pm1\%$	$q_\kappa^{\rm o}$ [e] $\pm2.2\%$	$q_\kappa^{\rm o+w}$ [f] $\pm2.3\%$
1	8.30	3.14	20.38	8.48	44.67	3.50	0.29	0.11	0.27	0.21	0.11	0.04
2	45.64	14.94	40.63	8.96	16.78	0.92	0.53	0.44	0.63	0.60	0.17	0.15
3	14.79	4.02	60.79	8.63	19.82	3.88	0.20	0.16	0.32	0.24	0.05	0.04
4	16.94	3.75	8.51	0.71	16.16	2.04	0.67	0.41	0.84	0.58	0.15	0.09
5	23.64	5.46	18.14	4.60	37.33	3.91	0.57	0.30	0.54	0.39	0.13	0.07
6	27.44	8.14	17.92	2.65	33.82	2.66	0.60	0.35	0.75	0.61	0.18	0.10
7	4.60	1.63	2.59	0.90	9.76	0.98	0.64	0.27	0.65	0.46	0.23	0.10
8	18.12	7.04	7.30	0.46	16.87	0.55	0.71	0.43	0.94	0.87	0.28	0.17
9	15.98	6.19	14.44	1.30	16.80	0.52	0.53	0.34	0.83	0.77	0.20	0.13
10	1.79	0.14	18.28	0.56	25.88	1.34	0.09	0.04	0.20	0.07	0.01	0
11	131.81	33.50	84.21	10.83	37.03	7.79	0.61	0.52	0.76	0.64	0.16	0.13
12	47.88	13.08	71.75	13.60	77.19	7.88	0.40	0.24	0.49	0.38	0.11	0.07
13	46.71	14.13	53.56	8.40	51.56	5.16	0.47	0.31	0.63	0.51	0.14	0.09
14	46.12	12.12	57.88	4.77	37.70	3.77	0.44	0.33	0.72	0.59	0.12	0.09
15	16.13	4.65	43.27	5.16	34.19	3.31	0.27	0.17	0.47	0.35	0.08	0.05
16	3.41	0.88	8.53	1.19	8.35	0.54	0.29	0.17	0.43	0.34	0.07	0.04
17	13.80	2.56	35.33	6.86	70.29	8.85	0.28	0.12	0.27	0.14	0.05	0.02
18	8.14	2.06	38.34	8.15	79.55	7.53	0.18	0.06	0.20	0.12	0.04	0.02
19	5.26	0.46	36.10	2.11	56.69	14.85	0.13	0.05	0.18	0.03	0.01	0
20	11.22	1.86	8.84	0.38	6.39	0.43	0.56	0.42	0.83	0.70	0.09	0.07
21	4.35	1.12	9.66	2.66	7.14	0.83	0.31	0.21	0.30	0.24	0.08	0.05
22	4.04	1.62	14.10	2.28	16.17	1.34	0.22	0.12	0.42	0.31	0.09	0.05
23	4.66	1.60	16.72	1.35	11.81	0.63	0.22	0.14	0.54	0.45	0.07	0.05
24	27.66	5.14	28.37	3.18	63.51	3.72	0.49	0.23	0.62	0.43	0.09	0.04
25	11.52	4.37	27.66	4.07	22.11	1.36	0.29	0.19	0.52	0.45	0.11	0.07
26	10.75	5.09	27.46	2.55	23.57	3.11	0.28	0.17	0.67	0.47	0.13	0.08
27	47.26	11.07	23.77	1.71	42.26	3.46	0.67	0.42	0.87	0.68	0.16	0.10
28	23.86	5.74	103.20	10.76	40.52	6.22	0.19	0.14	0.35	0.25	0.05	0.03
29	8.68	0.52	16.30	1.15	4.75	0.47	0.35	0.29	0.31	0.24	0.02	0.02
30	17.40	4.62	79.06	16.06	53.15	6.12	0.18	0.12	0.22	0.17	0.05	0.03
31	17.88	5.27	7.01	0.48	1.99	0.02	0.72	0.67	0.92	0.91	0.21	0.20
32	28.01	2.95	13.21	0.48	15.64	1.70	0.68	0.49	0.86	0.57	0.07	0.05
33	29.71	6.07	30.93	2.28	16.92	2.57	0.49	0.38	0.73	0.56	0.10	0.08
34	14.01	3.35	43.32	5.08	75.17	5.04	0.24	0.11	0.40	0.25	0.06	0.03
35	35.59	10.71	178.15	37.27	71.60	13.86	0.17	0.12	0.22	0.17	0.05	0.04
36	44.71	9.58	176.49	36.43	69.59	9.73	0.20	0.15	0.21	0.17	0.04	0.03
37	72.95	14.83	217.94	45.29	72.11	8.95	0.25	0.20	0.25	0.21	0.05	0.04
38	26.00	8.12	116.91	22.65	122.12	16.99	0.18	0.10	0.26	0.17	0.06	0.03
39	33.38	7.90	140.76	24.69	128.72	10.51	0.19	0.11	0.24	0.18	0.05	0.03
40	42.55	7.64	170.47	27.69	81.90	7.99	0.20	0.14	0.22	0.18	0.04	0.03
41	59.80	16.07	57.91	5.47	36.95	1.79	0.51	0.39	0.75	0.69	0.14	0.10
42	48.34	5.43	34.81	2.58	14.42	1.02	0.58	0.50	0.68	0.60	0.07	0.06
43	0.43	0.03	15.04	4.26	37.99	7.70	0.03	0.01	0.01	0	0	0
44	29.13	11.70	29.56	4.75	39.20	4.46	0.50	0.30	0.71	0.56	0.20	0.12
45	54.51	16.15	107.57	14.93	50.70	5.32	0.34	0.26	0.52	0.44	0.10	0.08
46	7.95	2.08	1.16	0.15	11.31	0.58	0.87	0.39	0.93	0.74	0.23	0.10
47	20.60	7.38	15.46	5.84	33.08	4.38	0.57	0.30	0.56	0.42	0.20	0.11
48	59.35	22.26	72.64	13.97	33.23	2.46	0.45	0.36	0.61	0.58	0.17	0.13
49	76.99	18.10	72.55	7.43	15.48	0.95	0.51	0.47	0.71	0.68	0.12	0.11
50	0	0	5.60	0.34	4.72	0.69	0	0	0	0	0	0
51	8.41	2.06	29.09	4.19	47.92	4.75	0.22	0.10	0.33	0.19	0.05	0.02

Notes.
[a] q_m calculated based on hypothesis 1 ($\Phi_{\rm surrounding} = \Phi_{\rm overlying,\ R}$).
[b] q_m calculated based on hypothesis 2 ($\Phi_{\rm surrounding} = \Phi_{\rm overlying,\ R} + \Phi_{\rm wall,\ R}$).
[c] q_τ calculated based on hypothesis 1 ($\Phi_{\tau\ \rm surrounding} = \Phi_{\tau\ \rm overlying,\ R}$).
[d] q_τ calculated based on hypothesis 2 ($\Phi_{\tau\ \rm surrounding} = \Phi_{\tau\ \rm overlying,\ R} + \Phi_{\tau\ \rm wall,\ R}$).
[e] q_τ calculated based on hypothesis 1 ($\Phi_{\rm surrounding} = \Phi_{\rm overlying,\ R}$).
[f] q_τ calculated based on hypothesis 2 ($\Phi_{\rm surrounding} = \Phi_{\rm overlying,\ R} + \Phi_{\rm wall,\ R}$).

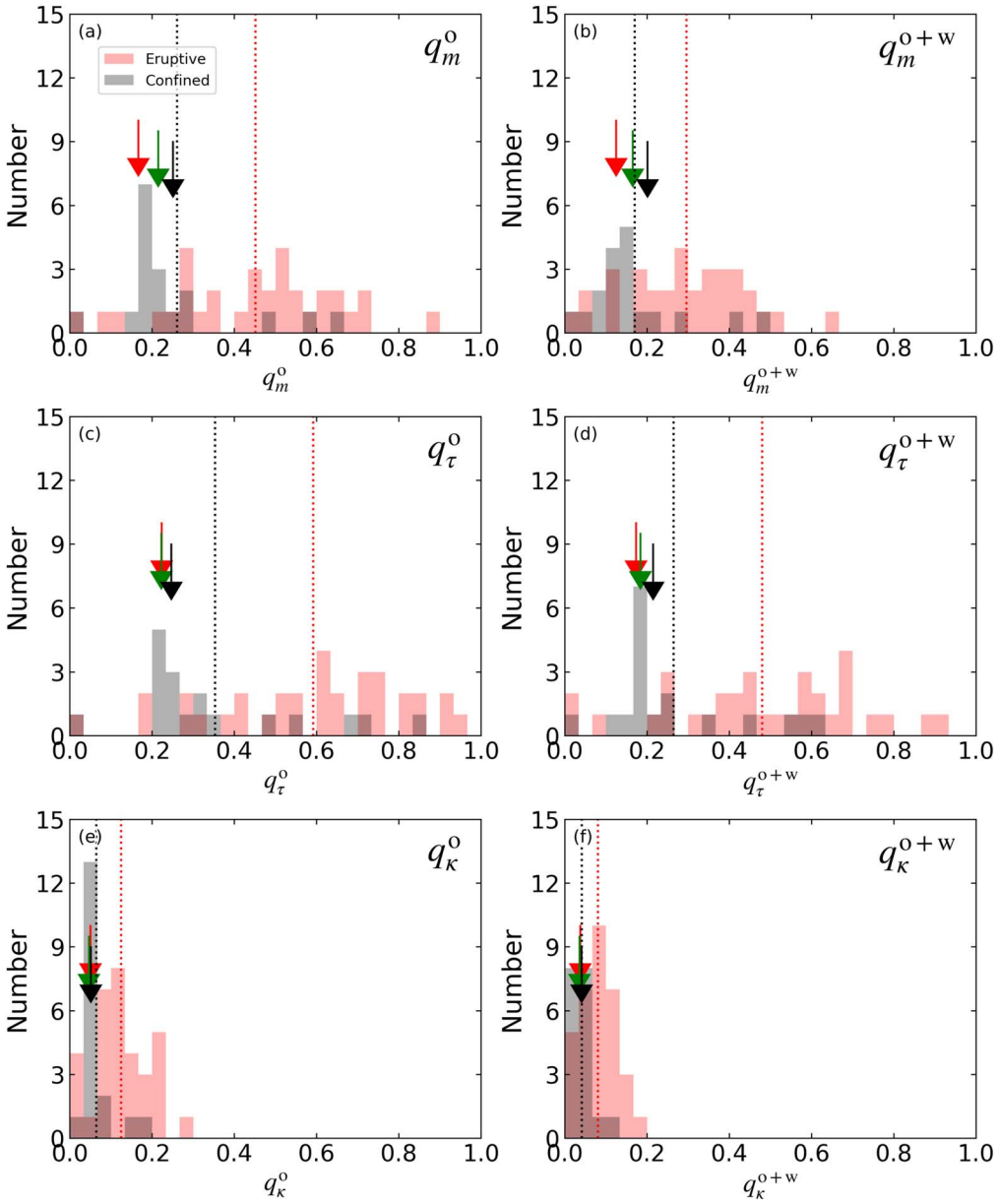

Figure 6. Histograms of (a) $q_m^{\rm o}$, (b) $q_m^{\rm o+w}$, (c) $q_\tau^{\rm o}$, (d) $q_\tau^{\rm o+w}$, (e) $q_\kappa^{\rm o}$, and (f) $q_\kappa^{\rm o+w}$ for eruptive events (red) and confined events (black). Red (black) vertical dashed lines indicate the mean value of the variables for eruptive (confined) events. The arrows colored in red, green, and black indicate the values for events #35, #36, and #37, respectively.

The statistical metrics for evaluating the distinguishing power of each parameter are summarized in Table 5. Within the bootstrap uncertainties, there is no significant difference between the *r*- and *q*-schemes for the MFR description, thus we cannot state which scheme is superior. All resulting DA metrics are also presented in Figure 3. The most significant difference between the two schemes is that the uncertainties of the *q*-scheme parameters as estimated by a Monte Carlo analysis are fairly small (see also Figure 3). For some metrics (e.g., all those corresponding to $q_m^{\rm o+w}$), the uncertainties are zero, owing to the fact that this estimate is basically inherited from the uncertainty listed in Table 4. In contrast, the bootstrap method provides larger uncertainties that reflect the small sample size; this can be regarded as the upper bound of uncertainty in the evaluation metrics for the *q*-scheme.

For context, we have made a comparison among parameters proposed by other studies that also aim to distinguish the eruptive and confined nature of flares. We use the data published in Wang et al. (2017), Baumgartner et al. (2018), Jing et al. (2018), and Duan et al. (2019), apply linear DA to the published data but, due to the different samples and sample sizes, only present the resulting probability that the samples are drawn from different populations (Table 6). We provide estimates of the associated uncertainties using the bootstrap method with 100 draws. The results in Table 6 demonstrate that the *r*- and *q*-scheme samples have a higher likelihood of being drawn from different populations (confined *versus* eruptive) compared to some proposed parameters. Other parameters of note include the $h_{\rm crit}$ (critical height defined according to the TI; Baumgartner et al. 2018 and Wang 2002), $\nabla\varphi$ (orientation change of the flare-related PIL with height; Baumgartner et al. 2018) $d_{\rm PC}$ (distance between flare site and flux-weighted AR center; Baumgartner et al. 2018), and decay index *n* from Duan et al. (2019) also show high probabilities of differentiating the

Table 5
DA Results (with $n-1$ Cross-validation)

Parameter	Method	Statistical Quantities			
		Probability[a]	MD[b]	CR[c]	TSS
$q_m^{\rm o}$	Original	98.2	1.03	0.80	0.55
	Monte Carlo	98.2 ± 0.0%	1.03 ± 0.00	0.78 ± 0.00	0.52 ± 0.00
	Bootstrap	93.3 ± 9.4%	1.05 ± 0.66	0.72 ± 0.08	0.29 ± 0.29
$q_m^{\rm o+w}$	Original	96.1	0.78	0.69	0.26
	Monte Carlo	96.1 ± 0.0%	0.78 ± 0.00	0.67 ± 0.00	0.21 ± 0.00
	Bootstrap	88.7 ± 15.0%	0.81 ± 0.56	0.69 ± 0.08	0.19 ± 0.26
$q_\tau^{\rm o}$	Original	98.2	1.04	0.76	0.48
	Monte Carlo	98.1 ± 0.5%	1.02 ± 0.07	0.74 ± 0.02	0.40 ± 0.06
	Bootstrap	94.0 ± 8.3%	1.08 ± 0.68	0.73 ± 0.07	0.32 ± 0.26
$q_\tau^{\rm o+w}$	Original	98.1	1.00	0.78	0.49
	Monte Carlo	98.1 ± 0.2%	1.01 ± 0.04	0.74 ± 0.01	0.42 ± 0.02
	Bootstrap	93.8 ± 8.0%	1.01 ± 0.59	0.72 ± 0.08	0.28 ± 0.27
$q_\kappa^{\rm o}$	Original	97.9	0.97	0.80	0.55
	Monte Carlo	98.2 ± 0.0%	1.03 ± 0.01	0.78 ± 0.00	0.52 ± 0.00
	Bootstrap	93.9 ± 7.6%	0.93 ± 0.52	0.71 ± 0.10	0.25 ± 0.32
$q_\kappa^{\rm o+w}$	Original	97.5	0.92	0.73	0.35
	Monte Carlo	96.2 ± 0.1%	0.78 ± 0.00	0.67 ± 0.00	0.21 ± 0.00
	Bootstrap	93.7 ± 7.0%	0.88 ± 0.47	0.69 ± 0.08	0.20 ± 0.26

Notes.
[a] Probability that the samples arise from different populations
[b] Mahalanobis distance for the sample PDFs.
[c] Correct rate of the classification table.

two populations and are comparable to those of the r- and q-schemes given the uncertainties from small sample sizes. While this comparison is interesting, it is limited; direct comparisons for further evaluation of these parameters should be performed on a common data set and preferably one with a significantly larger sample size overall.

In contrast to the r-scheme, the discrimination ability is not improved by the q-scheme when the wall field is included. We speculate that the intensity threshold for flare-ribbon regions should be considered to be an additional source of uncertainty. In Appendix D, we tested how the values of $\Phi_{\rm Ribbon}$, $\Phi_{\rm overlying,\ R}$, and $\Phi_{\rm wall,\ R}$ vary with adjustments of the intensity threshold, finding that the magnetic flux varies substantially for some events and shows no significant change for others. This implies an additional uncertainty with regard to the definition of flare ribbons. Despite these considerable uncertainties, these metrics provide a hint of how the propensity to erupt varies across different approximations of an MFR's location and boundaries.

Next, we discuss how the parameter values for events #35, #36, and #37 change across the distinct schemes. The values of all parameters for these target events are shown in Figures 2 and 6, and we find that the values of their r-scheme parameters decrease in the related q-scheme parameters. This can be confirmed by comparing the targets' values relative to the means of the distributions: the values are all close to the average in the r-scheme, whereas for the q-scheme, the values are smaller than the average.

To confirm the impact of using the flare-ribbon flux for the three targeted events, we summarize the ability of the two schemes to correctly classify them in Table 7, including $n-1$ cross-validation. We find that the q-scheme classifications, where the inferred sites of magnetic reconnection (flare ribbons) define the MFR, are in better agreement with the confined nature of these three events, particularly for $q_\tau^{\rm o}$, $q_\tau^{\rm o+w}$, and $q_\kappa^{\rm o}$. None of the r-scheme parameters provide a correct classification for these three events, hence we conclude that highly twisted flux ($|T_w| > 0.2$) provides an insufficient condition to identify the reconnected field lines.

4. Discussion

4.1. Critical Height Analysis

The TI (Kliem & Török 2006; Démoulin & Aulanier 2010) is an MHD instability described by force balance in the context of a coronal loop placed in an external magnetic field whose strength decreases with height. TI has been invoked in many studies to explain the eruptive properties of certain solar flares (e.g., Fan & Gibson 2007; Liu 2008; Guo et al. 2010; Nindos et al. 2012; Jing et al. 2015; Wang et al. 2017; Baumgartner et al. 2018; Duan et al. 2019). In this part, we investigate why the q-scheme can better classify the (non)eruptive nature of the three target events than can the r-scheme, from the viewpoint of this MHD instability.

The decay index n quantifies the falloff with height of the strapping force available to constrain an underlying magnetic flux rope (MFR):

$$n = -\frac{\partial \log B_{\rm h}}{\partial \log z}, \tag{11}$$

Table 6
Comparison of CME-eruptivity Judging Parameters

Parameter	Number of Eruptive Events	Number of Confined Events	Probability[a]
		Wang et al. (2017)	
$h_{\rm crit}$	35	25	$96.3 \pm 5.6\%$
		Jing et al. (2018)	
$E_{\rm free}$	26	12	$59.3 \pm 24.8\%$
$h_{\rm apex}$	26	12	$74.4 \pm 21.2\%$
d	26	12	$48.9 \pm 23.4\%$
n	26	12	$87.3 \pm 12.4\%$
$\lvert T_w\rvert$	26	12	$55.7 \pm 25.9\%$
$h_{\rm apex}/d$	26	12	$69.7 \pm 17.2\%$
		Baumgartner et al. (2018)	
Flux ratio	32	12	$71.2 \pm 13.3\%$
$d_{\rm FC}$	32	12	$82.5 \pm 19.5\%$
$d_{\rm PC}$	32	12	$92.6 \pm 12.8\%$
$h_{\rm crit}$	32	12	$100.0 \pm 0.0\%$
$\nabla\varphi$	19	9	$99.1 \pm 1.3\%$
		Duan et al. (2019)	
n	29	16	$92.1 \pm 10.8\%$
$\lvert T_w\rvert$	29	16	$43.3 \pm 26.3\%$
		Best-performing parameters of this analysis	
$r_\tau^{\rm o+w}$	33	18	$93.0 \pm 10.4\%$
$q_\tau^{\rm o}$	33	18	$94.0 \pm 8.3\%$
$q_\tau^{\rm o+w}$	33	18	$93.8 \pm 8.0\%$
$q_\kappa^{\rm o}$	33	18	$93.9 \pm 7.6\%$

Note.
[a] Probability that the samples arise from different populations. For all, a bootstrap with 100 draws was performed to estimate the uncertainty arising from the sample sizes.

where $B_{\rm h}$ is the horizontal component of the external magnetic field, and z represents the distance above the photosphere in the direction opposite gravity.

A critical height is defined as that where the corresponding n exceeds a critical value $n_{\rm c}$ and the strapping force can no longer constrain an MFR; the subsequent eruption will give rise to a CME. Analytic modeling indicates that $n_{\rm c}$ is typically between [1.1–2.0] (Bateman 1978; Kliem & Török 2006), and $n_{\rm c} = 1.5$ is widely used (e.g., Chen et al. 2015; Chintzoglou et al. 2017; Jing et al. 2018). Because the major difference between the q-scheme and the r-scheme is the distinct way of determining the MFR-relevant field lines (those in the flare-ribbon regions versus those with large T_w), the height that an inferred MFR can achieve could differ under these definitions. In this section, we compare the critical height derived for Events #35, #36, and #37 in the context of the two schemes and TI stability.

The TI analysis of the target events is outlined in Figure 7. For each event, n is calculated over the entire computational domain described in Appendix B. Of note, we use the potential field that initiates the NLFFF to estimate $B_{\rm h}$, and that model is provided roughly 1 hr before the GOES flare start time. By comparing the volume where the decay index is greater than a critical threshold (here $n > 1.5$) with the relevant extrapolated field lines, we can identify where the horizontal field is too weak to trap the MFR. We find volumes described by isocontours at $n = 1.5$ that provide "escape routes" of low-decay-index field by which MFRs could be directed upward, as an eruptive flare. These escape routes are reminiscent of the narrow channels of open flux discussed in DeRosa & Barnes (2018) in the context of CMEs, in that the complicated coronal magnetic topology can provide relatively small structures that could facilitate the escape of an MFR. In Figures 7(a)–(c), recalling that the target events are homologous flares as defined by the integrated flare ribbon areas, the configurations of the TI-unstable tunnels across the events are very similar. There are three TI-unstable tunnels in AR 12192, two tunnels are located in its periphery and one located near the central, major PIL.

To confirm the TI condition, the body of the MFR must lie underneath the height at which the decay index becomes critical, hence we also examine the vertical distribution of n. Figures 7(d)–(f) shows a cut of the vertical distribution of n in the context of the reconnection-imminent field lines as selected by the r- and q-schemes. Not surprisingly, the vertical distribution of n is similar across all three events, as are the field-line distributions. Those field lines identified with the MFR and as reconnection imminent according to the r-scheme by their $\lvert T_w\rvert \geqslant 0.2$ structure extend to a higher altitude and insert into the TI-unstable tunnel. The r-scheme classifies these events as eruptive, consistent with what would be expected in the context of the torus instability, but incorrect. Those field lines associated with the eventual flare ribbons, as defined by the q-scheme, do not reach as high in altitude and do not cross the $n \geqslant 1.5$ boundary or insert into the TI-unstable tunnel. The q-scheme's correct classification of "confined" is understood now in terms of this MHD instability as well.

We briefly examine whether, aside from NOAA AR 12192, "highly twisted field lines cannot represent a flux rope" is a general feature among other events that are misclassified by the r_m scheme. We surveyed the geometry of field lines in terms of the torus instability, following the analysis above, across 14 r_m-exceptional events, finding that

1. among six eruptive events, none has highly twisted field lines that exceed the $n > 1.5$ instability criterion, and
2. among eight confined events, four have highly twisted field lines that exceed the $n > 1.5$ instability criterion (three of those four being the target events discussed above).

As a result, we suggest that representing an MFR by the $\lvert T_w\rvert \geqslant 0.2$ threshold may have also caused a misclassification of other events originating from ARs besides AR 12192.

With the critical height study presented here, we find that the deduced eruptive potential is strongly dependent on the definition of the MFR. We see why the q-scheme performs better for the three target events, in that the real reconnected flux might be closer to the magnetic flux spatially associated with the flare ribbons. We find a substantial height difference between the field lines with $\lvert T_w\rvert \geqslant 0.2$ and those field lines associated with the flare ribbons. This difference implies that using the r-scheme to identify the eruption-imminent MFR could include field lines that are not responsible for the flare-triggering reconnection.

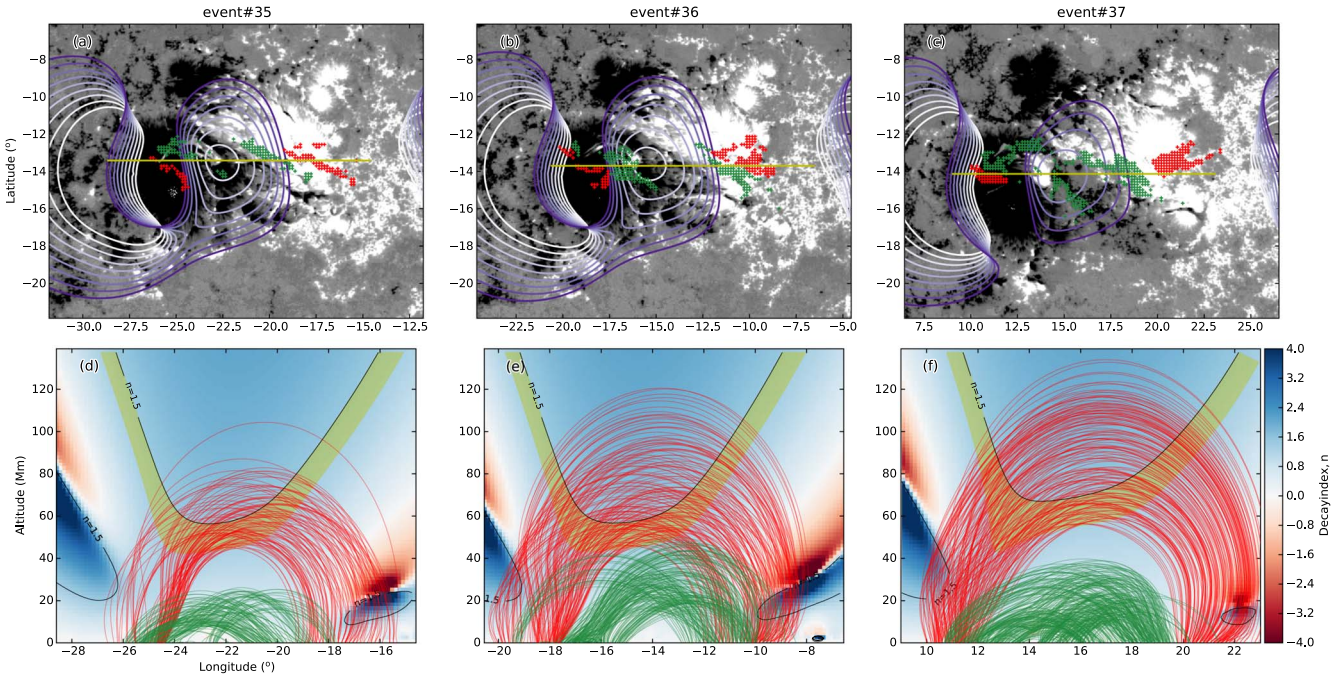

Figure 7. (a)–(c) Contour plot of decay index with height, overlaid on photospheric CEA B_r magnetograms saturated at ± 500 G. Marks correspond to the footpoints of the ribbon-associated-magnetic field lines (green) and the footpoints of the highly twisted ($|T_w| \geqslant 0.2$) field lines that have achieved the critical height (red), as indicated in panels (d)–(f). Areas within purple-white colored isocontours correspond to the area with $n = 1.5$ at seven selected equidistant height levels in the range between 50 and 80 Mm. (d)–(f) Vertical slices cut at the yellow lines in (a)–(c) show the distribution with height of n for each event, and the black contours indicate the critical height. Note that (d)–(f) only cover the extent of the yellow lines shown in (a)–(c). The translucent yellow area along with the black contours denotes the altitude corresponding to a critical value range $n = [1.3-1.5]$. The curves represent (red) all the projected field lines anchored in a highly twisted region ($|T_w| \geqslant 0.2$) that achieves the critical height ($n = [1.3-1.5]$, the yellow area shown) and (green) the projected field lines anchored in the flare ribbons.

Table 7
Comparison of DA Results across Different Schemes

event #	*r*-scheme						*q*-scheme					
	$r_m^{\rm o}$	$r_m^{\rm o+w}$	$r_\tau^{\rm o}$	$r_\tau^{\rm o+w}$	$r_\kappa^{\rm o}$	$r_\kappa^{\rm o+w}$	$q_m^{\rm o}$	$q_m^{\rm o+w}$	$q_\tau^{\rm o}$	$q_\tau^{\rm o+w}$	$q_\kappa^{\rm o}$	$q_\kappa^{\rm o+w}$
35	×	×	×	×	×	×	○	×	○	○	○	×
36	×	×	×	×	×	×	○	×	○	○	○	×
37	×	×	×	×	×	×	×	×	○	○	○	×

Note. ○: Correct Classification; ×: Misclassification.

4.2. Differences between the "Highly Twisted" Regions and the "Flare Ribbon" Regions

From the comparison of the *r*- and *q*-scheme based on the TI analysis, we surmise that appropriately determining the MFR could be crucial for classifying an event's eruptivity. We conclude that for some ARs/events, the MFR can be more appropriately approximated by the *q*-scheme (flare-ribbon field lines). Here we address a question: what makes T_w an insufficient condition for appropriately representing the MFR for some ARs/events?

The T_w is calculated using the linear integration of α along the full field line from the NLFFF model. Some field lines will meet the threshold of $|T_w| \geqslant 0.2$, with fairly low nonpotentiality (a small force-free constant α) but relatively long field-line length. As a result, even though T_w may serve as a good indication of the presence of an MFR, imposing the $|T_w| \geqslant 0.2$ threshold may fail to indicate the "volume" of the MFR, particularly in the target events.

To verify this hypothesis, in Figure 8, we examine the spatial distributions of T_w, field-line length (L), and α at the photosphere (the value for the corresponding field line). These maps are deduced from the NLFFF model 1 hr before the event. Across the maps for events #35, #36, and #37, the red contours mark the highly twisted region that has been determined by Paper I, the footpoints of field lines anchoring in the flare ribbons are indicated by green contours, and the two contours are coaligned according to solar differential rotation. In the T_w maps (Figures 8(a)–(c)), one can see that despite the flare ribbons being identified through a purely photometric method, they resemble the highly twisted regions in some parts: the flare ribbons and the twist number provide some consistent information regarding the location of the MFR, although the flare ribbons can only be mapped after the flare.

From the L maps (Figures 8(d)–(f)) compared to the flare-ribbon area, the "highly twisted regions" seem to stretch away from the PIL, corresponding to footpoints where the $T_w < -0.2$ is due primarily to the longer L. However, compared to L, it is difficult to distinguish any difference in the α distribution (Figures 8(g)–(i)) between the flare-ribbon area (green contours) and the highly twisted regions (red contours).

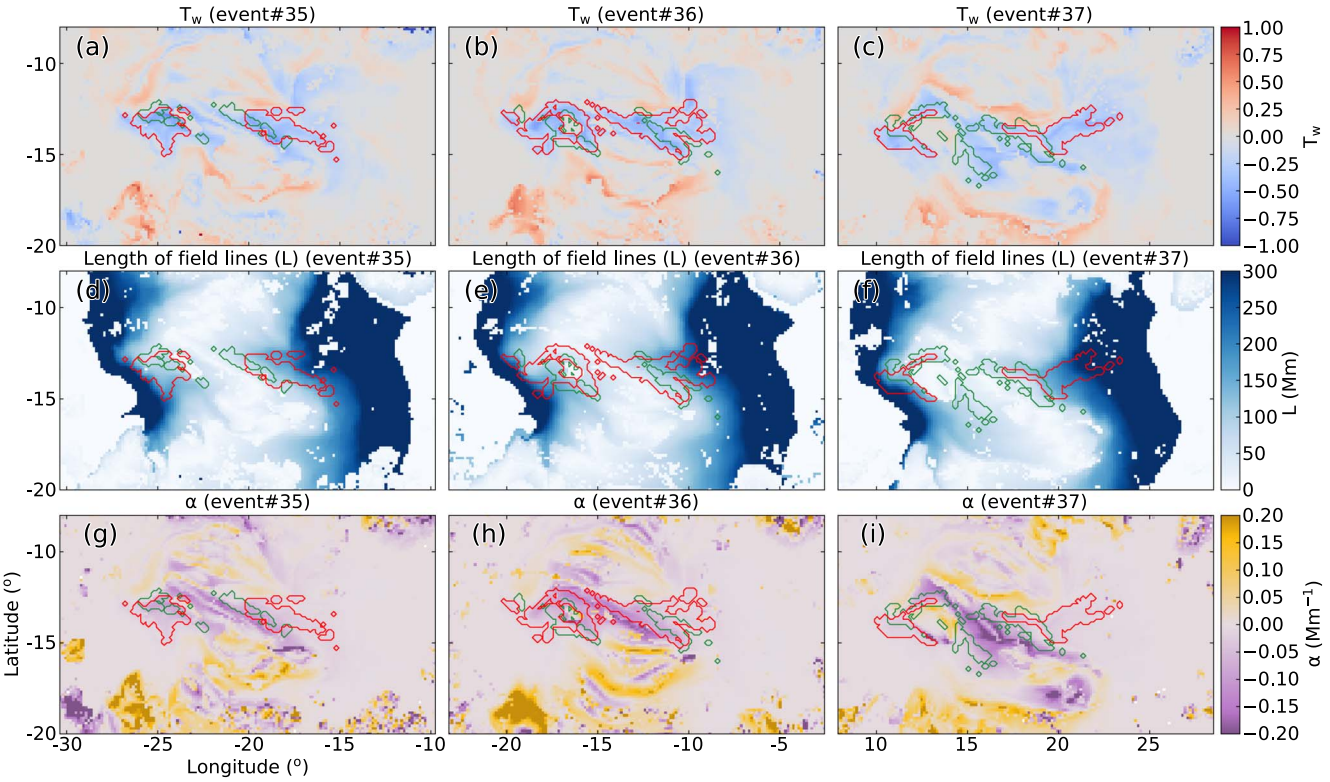

Figure 8. (a)–(c) Map of integrated twist T_w, (d)–(f) lengths of field lines (L), and (g)–(i) force-free constant (α) inferred from the NLFFF-extrapolated magnetic field model for events #35, #36, and #37. Red contours enclose the area with $|T_w| > 0.2$ that is used in calculating r parameters, and green contours enclose the footpoint area for field lines that have both footpoints anchored cospatially with the flare ribbons.

For a quantitative comparison, Figure 9 shows, for the three events, the distributions of L and α for the MFR-defining field lines identified by the r- and q-schemes. The temporal evolution of the flare ribbons is also indicated, as is the T_w threshold used in this study and in Lin et al. (2020). It is shown in Figure 9 that although the flare-ribbon field lines have predominantly $|T_w| \geqslant 0.2$, there are still some with $|T_w| < 0.2$. This implies that the reconnected field lines are not always highly twisted per our definition here.

The average L is larger for field lines in $|T_w| > 0.2$ and shorter than 150 Mm in length for the flare-ribbon-associated field lines. This implies that the flare-related reconnection mainly occurs on shorter field lines. The values of average α, on the other hand, show no significant difference between the two groups compared to the difference for the average L. This suggests that even field lines with small nonpotentiality could be involved in the reconnection process.

The temporal evolution of the flare ribbons presented in Figure 9 shows no consistent trend across the three events. For some details on the inconsistency of the ribbon progressions, a spatial depiction of the flare-ribbon evolution as seen in the AIA 1600 Å images is presented in Figure 10. We relate the progression shown in the α–L diagram (Figure 9) to the spatial progression (Figure 10) thus

1. *Event #35*: the initial brightening appears near longitude/latitude -25, -10.
2. *Event #36*: the initial brightening appears at multiple locations; hence, there is no obvious temporal trend in the α–L diagram.
3. *Event #37*: the ribbon patterns start near the PIL, gradually spreading away from it. The flare-related field lines gradually progress from high-α to low-α locations (as shown in Figure 8 (i)). This profile is consistent with the α–L diagram.

The results presented here suggest that the differing temporal evolution is due to the initial reconnection being activated at different locations. However, the coronal loops associated with the progressive reconnections share similar geometrical and topological features. As a result, the resulting flare ribbons are similar to each other in the integrated properties because the observed ribbons connect to these coronal loop structures at the corresponding footprints, even if they differ in some details.

With the distributions of α and L (Figure 9), we can compare the two schemes:

1. *Detecting/Defining the MFR*: field lines with $|T_w| \geqslant 0.2$ and lying near the PIL involved in the flare and near the flare ribbons in the r-scheme; flare-ribbon-related field lines in the q-scheme.
2. *α in the MFR*: no significant difference between the two schemes.
3. *L in the MFR*: no strong tendency across these three MFRs as defined by the r-scheme, while these MFRs as defined by the q-scheme are dominated by field lines with $L < 150$ Mm.

Because the q-scheme better represents the MFRs in these target events, we conclude that it is almost impossible to identify an MFR only based on nonpotentiality measures, for instance, α or T_w. We conclude that field-line length could be a good MFR identifier, as demonstrated for these three events. In summary, to estimate the total amount of reconnection contributed by an MFR, the geometrical information of field lines that compose the MFR is required in some events.

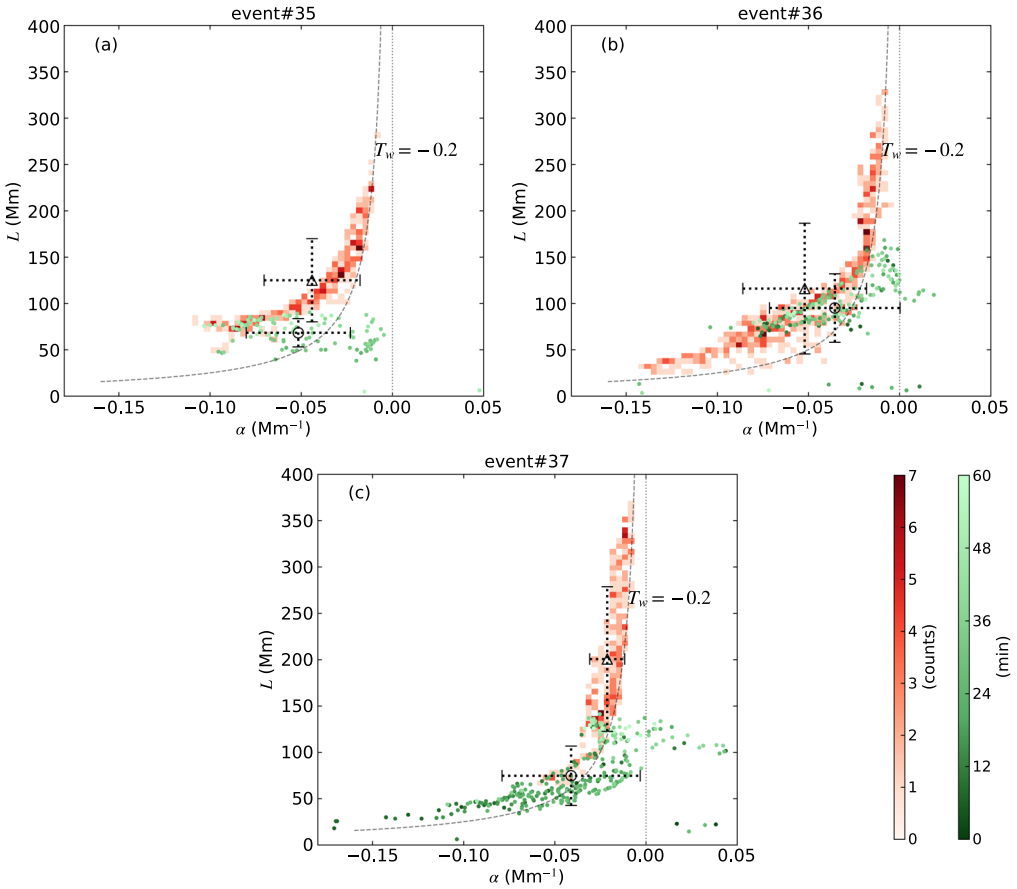

Figure 9. Diagram of α vs. L for (a) event #35, (b) event #36, and (c) event #37. The dots (green-white) indicate the locus for the flare-ribbon field lines (as identified for the q-scheme analysis) as a function of time (minutes after GOES start time listed in Table 1) when that field line's footpoint pixel first brightens in the AIA 1600 Å images. The underlying 2D histograms (red gradation) present the number density of the α–L distribution of field lines with $T_w < -0.2$ used in the r-scheme analysis. The average α and L for the $|T_w| > 0.2$ and flare-ribbon groups are indicated by the triangle and circle, respectively. The error bars indicate a $\pm\sigma$ spread. The dashed curve marks the $T_w = -0.2$ boundary.

5. Summary and Conclusions

The eruptive (or confined) nature of three solar flares originating from AR 12192, identified as events #35, #36, and #37 in Lin et al. (2020), failed to be correctly classified in that study using the original parameter r_m used to evaluate the MFR force balance in the context of its surrounding field. Here, we perform a systematic study on these three events to understand the factors that contributed to that failure. First, we propose that other physical quantities could better represent the force balance acting on the MFR. To test this hypothesis, we modified the r_m algorithm to incorporate instead the magnetic twist flux (Φ_τ), proposing two new parameters: r_τ and r_κ, which instead use the ratio of the magnetic twist flux and the ratio of magnetic twist flux to magnetic flux, respectively. Second, we further proposed that the area defined by field lines showing greater than 0.2 winds ($|T_w| \geqslant 0.2$) may insufficiently represent the MFR.

Taking a different tack, we then suggest that using the information on the flare-ribbon location and evolution may provide a more direct approximation of the reconnected magnetic flux, that is, would better identify those field lines that comprise the MFR. Mirroring the r-scheme and its parameters r_m, r_τ, and r_κ, we propose the q-scheme based on the flare-ribbon-associated magnetic field, and parameters q_m, q_τ, and q_κ. In the q-scheme, the highly twisted field lines used in the r-scheme are replaced by field lines whose footpoints are cospatial with flare ribbons as identified using AIA 1600 Å image sequences.

Linear discriminant analysis was used to classify all 51 of the events for all parameters from both r- and q-schemes (Section 2.4). Quantitative metrics are then used to evaluate the parameters' classification success. The resulting DA metrics demonstrate that both schemes have a "moderate" classification ability overall, with large uncertainties due primarily to the small sample size. For the three target events, none of the parameters in the r-scheme, including the new ones, provide correct classification outcomes. Conversely, as summarized in Table 7, three of the six q-scheme correctly classify the three target events' eruptivities.

To investigate this performance difference for the three target events, we invoke an analysis based on the torus instability, comparing the height where the decay index reaches critical levels to the height reached by the relevant magnetic field lines in the two schemes. We find that when using the flare-ribbon-related field lines to approximate the target MFR, TI can correctly classify confined events; the result is consistent with the result inferred from the q-scheme, which also uses the flare-ribbon-related field lines to assume the volume of the MFR. On the other hand, when using field lines with $|T_w| \geqslant 0.2$ to approximate the MFR, TI incorrectly classifies eruptive events; the result is consistent with the eruptivity inferred by

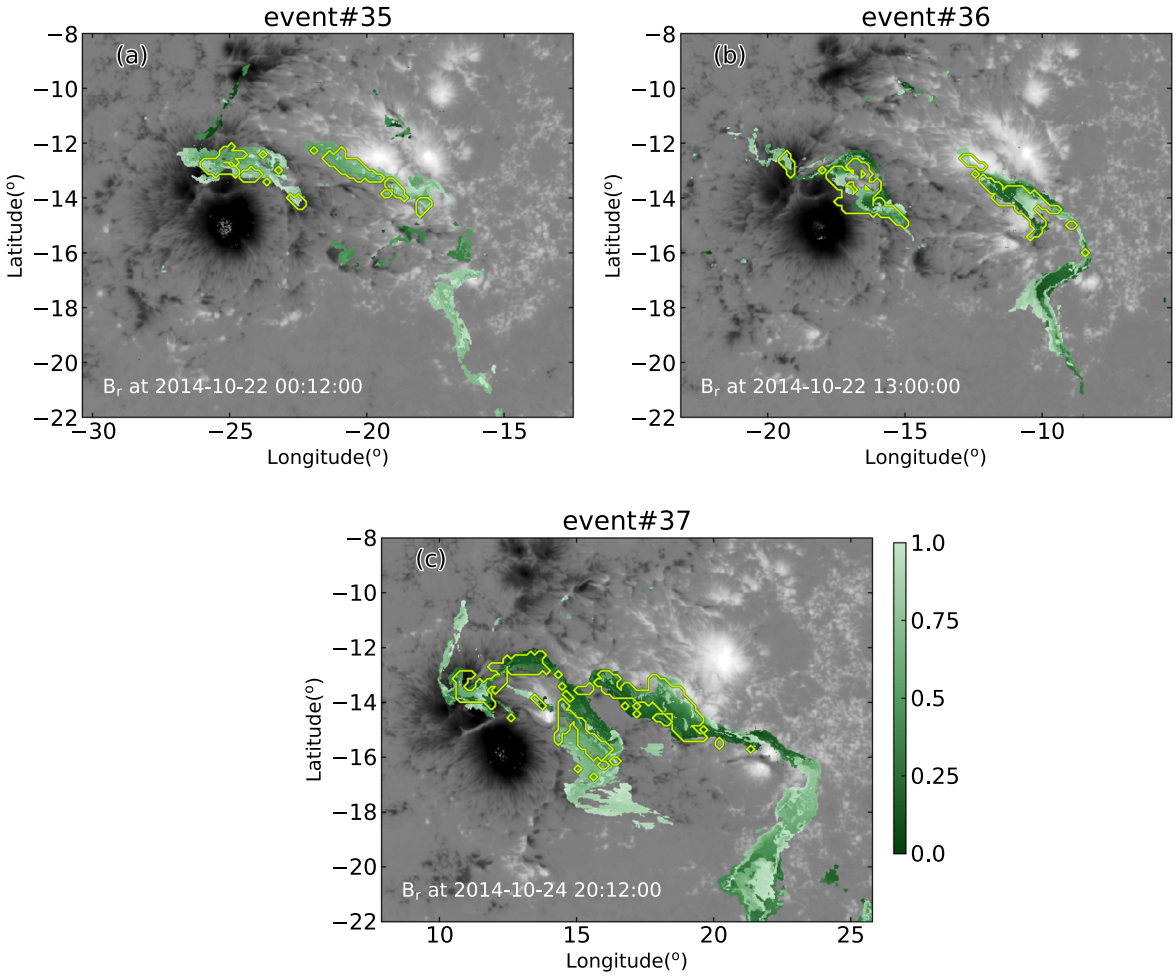

Figure 10. Temporal evolution of flare ribbons overlaid on the SHARP B_r magnetogram (from ≈1 hr before the flare onset and saturated at ±2500 G) for (a) event #35, (b) event #36, and (c) event #37. The color is assigned according to when the flare-ribbon pixel first appears in AIA 1600 Å images from the GOES start time up to the GOES peak time listed in Table 1, which is normalized to between [0, 1]. The light-green contours highlight the pixels included in calculating the *q*-scheme parameters.

the *r*-scheme, which also uses the highly twisted field lines to approximate the MFR. This exercise of comparing the expected eruptivities from two entirely distinct methods emphasizes the importance of correctly separating the volume of an MFR from the ambient magnetic field.

The analysis so far demonstrates that any MFRs existing in the target events are improperly represented by the field having more than 0.2 turns. To search for field lines with twist number exceeding 0.2 turns but that contain inadequate nonpotentiality, our α–L diagram (Figure 9) shows the distributions of the force-free parameter α and NLFFF-model field-line length L for the two distinct groups of field lines. Counterintuitively, we find no obvious difference between the two schemes' field lines in terms of the distribution of α, implying almost equal nonpotentiality among them across the target events. However, all of the flare-ribbon-associated field lines are shorter than 150 Mm in length, while the *r*-scheme defined field lines appear with a wide range of lengths, $25 \gtrsim L \gtrsim 380$ Mm. This finding leads us to conclude that the event-triggering reconnections for these events are restricted to shorter, although not necessarily highly nonpotential, field lines.

The temporal behaviors of the flare ribbons shown in the α–L diagrams suggest that there is no consistent tendency in the temporal evolution of these three flares. We examine the flare-ribbon behaviors in detail through time sequences of SDO/AIA 1600 Å filtergrams, presenting the flares' progressions in Figure 10. We find that the target events' onset reconnections begin at different locations but are associated with similar coronal magnetic field systems. These differences in ribbon evolution are notable in that, otherwise, the three flares appear homologous.

In summary, we contend that for these three events, the factor behind their incorrect classification in the *r*-scheme is the incorrect identification of the volume of the MFRs. Admittedly, the physical quantities involving nonpotentiality (i.e., T_w or α) may be useful to indicate the presence of an MFR. However, employing a strict twist threshold (here $|T_w| \geqslant 0.2$), or other parameters based on common measures of magnetic nonpotentiality, can be an insufficient condition for isolating the main body of an MFR, and the correct identification of the MFR can greatly impact any prediction of an event's associated CME production. Moreover, although the *q*-scheme correctly classified the 3 target events whereas the *r*-schemes had failed, overall, for the 51 events studied, the classification performance stayed the same between the two schemes, with a moderate level of success. We propose that there is likely to be

more than one mechanism governing CME production. Finally, the results presented in this study demonstrate that the argument regarding whether a flare will erupt with a CME or not should be redefined as a question of how to accurately extract the relevant MFR characteristics from the observations.

We thank the SDO HMI and AIA teams for providing the vector magnetic field and EUV data used in this study. We acknowledge Dr. Graham Barnes for invaluable comments that improved this paper. This work was supported by MEXT/JSPS KAKENHI grant No. JP15H05814. A part of this work was carried by using the computational resource of the Center for Integrated Data Science, Institute for Space-Earth Environmental Research (ISEE), Nagoya University. Visualization of the NLFFF is produced by VAPOR (Clyne & Rast 2005; Clyne et al. 2007). The Discriminant Analysis code was developed by Dr. Graham Barnes of NorthWest Research Associates (NWRA). K.D.L. acknowledges support from NWRA and the US National Science Foundation under grant Nos. 1630454 and 1841962; any opinions, findings, and conclusions or recommendations expressed in this material are those of the authors and do not necessarily reflect the views of the National Science Foundation. P.L. acknowledges the Japan-Taiwan Exchange Association for supporting this study and stay in Nagoya University.

Appendix A
Event List

We use in this study an identical event list to that in Paper I, originally proposed by Toriumi et al. (2017). Details on the flare event start time, GOES class, location, NOAA AR#, and whether or not the event was accompanied by a CME are all given in Lin et al. (2020, Table 1) and not reproduced here.

Appendix B
Nonlinear Force-free Field Reconstruction

In this study, NLFFF models are implemented to reconstruct the coronal magnetic field structure. An MHD relaxation method developed by Inoue et al. (2014) was extended to work in spherical coordinates as required for this study. We applied the `INTERPOLATION` function of IDL to reduce the resolution of the magnetogram to $0.14^\circ \times 0.14^\circ$ in each pixel for the lower boundary of the NLFFF extrapolation. The potential field is required as the initial condition and boundary condition of the extrapolation, for which the potential field source-surface (PFSS) model (Altschuler & Newkirk 1969; Shiota et al. 2008) is initiated using a modified HMI synoptic chart of radial magnetic field (`hmi.Synoptic_Mr_720s`). The synoptic charts are generated after every Carrington Rotation ($\sim$27 days) is completed, hence we replace the target region with the SHARP boundary data to ensure accuracy within the area under immediate consideration. The PFSS is then calculated using a 1024-order spherical harmonic series expansion from the lower boundary (the modified synoptic chart) to a height of 2.5 solar radii. From this PFSS model, we cropped out the wedge defined by the area of embedded SHARP data; at the lower base of the domain, the resolution is 0.0025 $R_\odot$ per cell. From this PFSS wedge, the MHD-relaxation method is invoked and gradually changes the horizontal components of the boundary field (B_θ and B_ϕ) through a set of MHD-like equations, but B_r remains unchanged. We stop the iteration when the best-fit solution for all physical variables is achieved at all boundaries. The Lorentz force and the solenoidal condition within the numerical box are evaluated at the final step. Finally, we numerically derive the three-dimensional coronal magnetic field using a fourth-order Runge–Kutta-Gill scheme for the temporal integrals and a second-order central finite difference scheme for the spatial derivatives. Metrics that evaluate the NLFFF models themselves are provided in Lin et al. (2020, Table A1).

Appendix C
Error Analysis

We evaluated the expected sensitivity to the uncertainty in the magnetic boundary data through a Monte Carlo analysis of one event (event #1) and assume that the results are representative of expected data-imposed uncertainties for the analysis of the other 50 events. For event #1, reported uncertainties are provided in the `hmi.sharp_cea_720s` segments: `Br_err.fits`, `Bp_err.fits`, and `Bt_err.fits`. The uncertainty at each pixel is multiplied by a random number generated from a distribution with a normal distribution and unity variance, and added to the magnetogram used as the lower boundary of NLFFF extrapolation. The whole process was repeated 16 times to obtain 16 sets of NLFFF data with different fluctuations as per realizations of the noise. We consequently estimate the variables that are used in this study (e.g., $\Phi_{|T_w|\geq 0.2}$, etc.) using these data sets and derive the corresponding standard deviation across all 16 data sets. These standard deviations provide the percentage errors quoted in Tables 2, 4.

To test the reliability of the DA metrics, we estimate their uncertainties by two methods: (1) the Monte Carlo method to estimate the errors that arise from the errors in the data, and (2) a bootstrap algorithm to indicate the uncertainties that arise from the small sample size.

For (1) the Monte Carlo method, the uncertainties for each parameter are inherited from the uncertainties of Φ and Φ_τ as described above. We perform the DA on 10,000 sets of each parameter wherein, for each set, uncertainties are added based on Gaussian-distributed random numbers. The standard deviation of the error values of Φ or Φ_τ are used to calculate the corresponding values of parameters in the *r*-scheme and the *q*-scheme. The uncertainties from this method are generally quite small.

The bootstrap method (2) provides uncertainty levels that arise from the sampling process. We reconstruct the samples by drawing (with replacement) 51 samples from the original data set to obtain different realizations. Each realization thus may include repeated samples and present a different event rate. We repeat this resampling procedure 100 times and obtain 100 sets of resulting DA metrics from which we calculate the standard deviation, and report it as the uncertainty in that metric.

Appendix D
Flare-ribbon Area Sensitivity to Different Intensity Thresholds

An intensity threshold is defined for AIA 1600 Å observations above which we label pixels as having brightened sufficiently to be included as part of the "flare ribbons." This 1600 Å intensity threshold is empirically imposed as 20σ above the mean 1600 Å intensity at a flare-quiet time. This brings us

Table 8
Maximum Variation Rate across Intensity Thresholds $n \in [10, 30]\sigma$

Event#	$\Delta\Phi_{\mathrm{Ribbon},n\sigma}$	$\Delta\Phi_{\mathrm{overlying,R},n\sigma}$	$\Delta\Phi_{\mathrm{wall,\ R},n\sigma}$
1	1.91	0.19	0.16
2	0.54	0.38	0.02
3	1.51	0	0.30
4	0.27	0.68	1.16
5	0.42	0.25	0
6	0.61	0.93	1.15
7	0.37	1.61	4.70
8	0.15	1.85	0.74
9	0.50	0.67	0.34
10	4.12	1.46	2.36
11	0.28	1.00	0
12	1.73	0.85	0
13	0.13	0.40	0.03
14	0.43	0.25	0.22
15	0.34	0.74	0.59
16	0.85	0.46	3.19
17	0.55	0.14	0.20
18	0.80	0.34	0.34
19	2.00	1.93	1.64
20	0.49	1.23	0.23
21	1.17	0.50	0.14
22	0.65	0.97	0.38
23	0.34	0.72	0.01
24	0.12	0.17	0.80
25	0.04	0.14	0.02
26	0.08	0.18	0
27	0.05	0.95	0.01
28	1.01	0.19	0.03
29	0.45	1.58	2.01
30	0.57	0.09	0.01
31	0.23	0.39	0.18
32	0.22	0.36	0
33	0.77	0.77	0
34	0.61	0.08	0.31
35	0.78	0.38	0.23
36	0.34	0	0
37	0.47	0.65	0.30
38	0.33	0.30	0
39	0.88	0.70	0.06
40	0.87	0.70	0.16
41	0.20	0.21	0
42	0.16	0.70	0.06
43	7.77	0.23	1.06
44	0.85	0.22	0
45	0.71	0.32	0.01
46	0.26	2.80	5.39
47	0.43	0.34	0.30
48	0.65	0.27	0
49	0.30	0.38	0.10
50	0	1.14	0.04
51	0.26	0.46	0

to the question: to what extent does the choice of the threshold affect the resulting flare-ribbon area and associated magnetic flux calculations?

To answer this question, we adjust the threshold across 10σ–30σ, and from the resulting flare-ribbon masks, we calculate the corresponding values of Φ_{Ribbon}, $\Phi_{\mathrm{overlying,\ R}}$, and $\Phi_{\mathrm{wall,\ R}}$ following the method outlined in Section 3.2. We consequently calculate the differences in the yielded values relative to those calculated using the 20σ threshold, where the variation is defined as

Table 9
Averaged DA Metrics Vary with Different n

	Statistical Quantities			
n	Probability[a]	MD[a]	CR[b]	TSS
10	98.0	1.09	0.76	0.46
15	98.2	1.07	0.76	0.45
20	97.7	0.96	0.76	0.45
25	95.7	0.74	0.69	0.26
30	95.5	0.73	0.66	0.20

Notes.
[a] Probability that the samples arise from different populations.
[b] Mahalanobis distance for the sample PDFs.
[c] Correct rate of the classification table.

$$\Delta\Phi_{\mathrm{Ribbon},n\sigma} = \frac{|\Phi_{\mathrm{Ribbon},n\sigma} - \Phi_{\mathrm{Ribbon},20\sigma}|}{\Phi_{\mathrm{Ribbon},20\sigma}}, \quad \text{(D1)}$$

where $\Phi_{\mathrm{Ribbon,n}\sigma}$ indicates the flare-ribbon-related magnetic flux calculated with the intensity threshold at $n\sigma$ above the mean quiet 1600 intensity. The maximum variation among the values derived with $n \in [10, 30]\sigma$ is provided in Table 8. Mirroring the estimation of $\Delta\Phi_{\mathrm{Ribbon},n\sigma}$, we calculate $\Delta\Phi_{\mathrm{overlying,\ R},n\sigma}$ and $\Delta\Phi_{\mathrm{wall,\ R},n\sigma}$ as

$$\Delta\Phi_{\mathrm{overlying,\ R},n\sigma} = \frac{|\Phi_{\mathrm{overlying,\ R},n\sigma} - \Phi_{\mathrm{overlying,\ R},20\sigma}|}{\Phi_{\mathrm{overlying,\ R},20\sigma}}, \quad \text{(D2)}$$

$$\Delta\Phi_{\mathrm{wall,\ R},n\sigma} = \frac{|\Phi_{\mathrm{wall,\ R},n\sigma} - \Phi_{\mathrm{wall,\ R},20\sigma}|}{\Phi_{\mathrm{wall,\ R},20\sigma}}. \quad \text{(D3)}$$

The maximum variation of the overlying-field and wall-field term is also listed in Table 8. We find that the variation can reach seven times the original flux (Φ_{Ribbon} in event #43), although sometimes the values change minimally (e.g., event #25). In general, the flare-ribbon magnetic flux varies between 10% and 90% from what was used in the present analysis, indicating a fairly strong sensitivity to the empirical threshold used to determine what constitutes a flare ribbon. We note that this large uncertainty is consistent with the conclusions of the paper regarding the difficulty of determining the MFR characteristics.

From relevant literature, Qiu et al. (2010) noted that the "steady-state" UV brightening associated with plage regions is generally at 3.5 times the background median value. A threshold set at 10σ above the mean intensity will typically be greater than this value. As a result, we expect that an intensity threshold at least $\geqslant 10\sigma$ above the background mean intensity would be suitable to capture the major morphology of flare ribbons. Besides the 20σ threshold applied herein, Toriumi et al. (2017) applied a threshold intensity at 40σ above the quiet-Sun mean values; Kazachenko et al. (2017) used thresholds ranging from 6–10 times above the background median value. These thresholds are all substantially greater than that suggested by Qiu et al. (2010).

Next, we discuss which threshold is most appropriate for this study. We apply DA on the parameters as yielded by the threshold intensity at $n\sigma$ above the mean values, adjusting n across 10–30, to see how the discrimination ability changes across different values of n. Table 9 shows the DA metrics used, averaged across all q-scheme parameters, as they vary

with n. The quantities listed demonstrate that the averaged DA metrics show comparative performance when $n \in [10, 20]$, while the performance drastically decreases at and beyond $n = 25$. Therefore, we elect $n = 20$ in our analysis such that we will not underestimate the performance of the q-scheme.

ORCID iDs

Pei Hsuan Lin https://orcid.org/0000-0002-3873-7599
Kanya Kusano https://orcid.org/0000-0002-6814-6810
K. D. Leka https://orcid.org/0000-0003-0026-931X

References

Alexander, D., Liu, R., & Gilbert, H. R. 2006, ApJ, 653, 719
Altschuler, M. D., & Newkirk, G. 1969, SoPh, 9, 131
Antiochos, S. K., DeVore, C. R., & Klimchuk, J. A. 1999, ApJ, 510, 485
Bamba, Y., Lee, K.-S., Imada, S., & Kusano, K. 2017, ApJ, 840, 116
Bateman, G. 1978, MHD Instabilities (Cambridge, MA: MIT Press)
Baumgartner, C., Thalmann, J. K., & Veronig, A. M. 2018, ApJ, 853, 105
Berger, M. A., & Prior, C. 2006, JPhA, 39, 8321
Bobra, M. G., & Ilonidis, S. 2016, ApJ, 821, 127
Burlaga, L. F. 1991, Physics of the Inner Heliosphere II (Berlin: Springer), 1
Carmichael, H. 1964, in AAS NASA Symp. Physics of Solar Flares, NASA SP-50 (Washington, DC: NASA), 451
Chen, H., Zhang, J., Ma, S., et al. 2015, ApJL, 808, L24
Chen, J., Howard, R., Brueckner, G., et al. 1997, ApJL, 490, L191
Cheng, X., Zhang, J., Ding, M. D., Guo, Y., & Su, J. T. 2011, ApJ, 732, 87
Cheng, X., Zhang, J., Ding, M. D., & Poomvises, W. 2010, ApJ, 712, 752
Chintzoglou, G., Vourlidas, A., Savcheva, A., et al. 2017, ApJ, 843, 93
Clyne, J., Mininni, P., Norton, A., & Rast, M. 2007, NJPh, 9, 301
Clyne, J., & Rast, M. 2005, Proc. SPIE, 5669, 284
Démoulin, P., & Aulanier, G. 2010, ApJ, 718, 1388
Dere, K., Brueckner, G., Howard, R., Michels, D., & Delaboudiniere, J. 1999, ApJ, 516, 465
DeRosa, M. L., & Barnes, G. 2018, ApJ, 861, 131
Duan, A., Jiang, C., He, W., et al. 2019, ApJ, 884, 73
Einaudi, G., & Hoven, G. V. 1983, SoPh, 88, 163
Fan, Y., & Gibson, S. E. 2007, ApJ, 668, 1232
Filippov, B. 2020, MNRAS, 494, 2166
Forbes, T. 2000, JGRA, 105, 23153
Gary, G. A. 2001, SoPh, 203, 71
Gibson, S., & Fan, Y. 2006, ApJL, 637, L65
Green, L. M., & Kliem, B. 2009, ApJL, 700, L83
Green, L. M., Kliem, B., & Wallace, A. 2011, A&A, 526, A2
Guo, Y., Ding, M. D., Schmieder, B., et al. 2010, ApJL, 725, L38
Hanssen, A., & Kuipers, W. 1965, Meded. Verhand., 81, 2
Harrison, R. 1995, A&A, 304, 585
Harrison, R. 2003, AdSpR, 32, 2425
Hills, M. 1966, RSPSB, 28, 1
Hirayama, T. 1974, SoPh, 34, 323
Hood, A. W., & Priest, E. R. 1979, SoPh, 64, 303
Inoue, S., Hayashi, K., & Kusano, K. 2016, ApJ, 818, 168
Inoue, S., Hayashi, K., Magara, T., Choe, G. S., & Park, Y. D. 2014, ApJ, 788, 182
Ishiguro, N., & Kusano, K. 2017, ApJ, 843, 101
Ji, H., Wang, H., Schmahl, E. J., Moon, Y.-J., & Jiang, Y. 2003, ApJL, 595, L135
Jiang, C., Wu, S. T., Yurchyshyn, V., et al. 2016, ApJ, 828, 62
Jing, J., Liu, C., Lee, J., et al. 2018, ApJ, 864, 138
Jing, J., Xu, Y., Lee, J., et al. 2015, RAA, 15, 1537
Kazachenko, M. D., Lynch, B. J., Welsch, B. T., & Sun, X. 2017, ApJ, 845, 49
Kliem, B., & Török, T. 2006, PhRvL, 96, 255002
Kopp, R., & Pneuman, G. 1976, SoPh, 50, 85
Kuridze, D., Mathioudakis, M., Kowalski, A., et al. 2013, A&A, 552, A55
Kusano, K., Iju, T., Bamba, Y., & Inoue, S. 2020, Sci, 369, 587
Kushwaha, U., Joshi, B., Veronig, A. M., & Moon, Y.-J. 2015, ApJ, 807, 101
Leka, K., Fan, Y., & Barnes, G. 2005, ApJ, 626, 1091
Leka, K. D., & Barnes, G. 2003, ApJ, 595, 1296
Lemen, J. R., Akin, D. J., Boerner, P. F., et al. 2011, The Solar Dynamics Observatory (Berlin: Springer), 17
Li, T., Hou, Y., Yang, S., et al. 2020, ApJ, 900, 128
Lin, J., & Forbes, T. G. 2000, JGR, 105, 2375
Lin, P. H., Kusano, K., Shiota, D., et al. 2020, ApJ, 894, 20
Liu, R., Kliem, B., Titov, V. S., et al. 2016, ApJ, 818, 148
Liu, Y. 2008, ApJL, 679, L151
Liu, Y., Su, J., Xu, Z., et al. 2009, ApJL, 696, L70
Maričić, D., Vršnak, B., Stanger, A. L., et al. 2007, SoPh, 241, 99
Moore, R. L., Sterling, A. C., Hudson, H. S., & Lemen, J. R. 2001, ApJ, 552, 833
Muhamad, J., Kusano, K., Inoue, S., & Bamba, Y. 2018, ApJ, 863, 162
Munro, R., Gosling, J., Hildner, E., et al. 1979, SoPh, 61, 201
Nindos, A., Patsourakos, S., & Wiegelmann, T. 2012, ApJL, 748, L6
Pagano, P., Mackay, D. H., & Yardley, S. L. 2019, ApJ, 883, 112
Panesar, N. K., Sterling, A. C., & Moore, R. L. 2016, ApJL, 822, L23
Prasad, A., Bhattacharyya, R., Hu, Q., Kumar, S., & Nayak, S. S. 2018, ApJ, 860, 96
Priest, E., & Démoulin, P. 1995, JGR, 100, 23443
Priest, E., & Forbes, T. 2002, A&ARv, 10, 313
Qiu, J., Liu, W., Hill, N., & KAZACHENkO, M. 2010, ApJ, 725, 319
Qiu, J., Liu, W.-J., & Longcope, D. W. 2012, ApJ, 752, 124
Sarkar, R., & Srivastava, N. 2018, SoPh, 293, 1
Savcheva, A. S., Green, L. M., van Ballegooijen, A. A., & DeLuca, E. E. 2012, ApJ, 759, 105
Sheeley, N., Jr, Howard, R., Koomen, M., & Michels, D. 1983, ApJ, 272, 349
Shiota, D., Kusano, K., Miyoshi, T., Nishikawa, N., & Shibata, K. 2008, JGRA, 113, A03S05
Sturrock, P. 1966, Natur, 211, 695
Sun, X., Bobra, M. G., Hoeksema, J. T., et al. 2015, ApJL, 804, L28
Temmer, M., Veronig, A. M., Vršnak, B., et al. 2008, ApJL, 673, L95
Thalmann, J., Su, Y., Temmer, M., & Veronig, A. 2015, ApJL, 801, L23
Thalmann, J. K., Moraitis, K., Linan, L., et al. 2019, ApJ, 887, 64
Toriumi, S., Schrijver, C. J., Harra, L. K., Hudson, H., & Nagashima, K. 2017, ApJ, 834, 56
Török, T., & Kliem, B. 2005, ApJL, 630, L97
Tschernitz, J., Veronig, A. M., Thalmann, J. K., Hinterreiter, J., & Pötzi, W. 2018, ApJ, 853, 41
van der Walt, S., Schönberger, J. L., Nunez-Iglesias, J., et al. 2014, PeerJ, 2, e453
Veronig, A., & Polanec, W. 2015, SoPh, 290, 2923
Vourlidas, A., Lynch, B. J., Howard, R. A., & Li, Y. 2013, SoPh, 284, 179
Wang, D., Liu, R., Wang, Y., et al. 2017, ApJL, 843, L9
Wang, Y., & Zhang, J. 2007, ApJ, 665, 1428
Wang, Y. M. 2002, JGRA, 107, 1340
Webb, D., & Hundhausen, A. 1987, SoPh, 108, 383
Zhang, J., & Dere, K. 2006, ApJ, 649, 1100
Zhang, J., Dere, K. P., Howard, R. A., Kundu, M. R., & White, S. M. 2001, ApJ, 559, 452